

LOCALIZATION AND GEOMETRIZATION IN PLASMON RESONANCES AND GEOMETRIC STRUCTURES OF NEUMANN-POINCARÉ EIGENFUNCTIONS

EEMELI BLÅSTEN, HONGJIE LI, HONGYU LIU, AND YULIANG WANG

ABSTRACT. This paper reports some novel and intriguing discoveries about the localization and geometrization phenomenon in plasmon resonances and the intrinsic geometric structures of Neumann-Poincaré eigenfunctions. It is known that plasmon resonance generically occurs in the quasi-static regime where the size of the plasmonic inclusion is sufficiently small compared to the wavelength. In this paper, we show that the global smallness condition on the plasmonic inclusion can be replaced by a local high-curvature condition, and the plasmon resonance occurs locally near the high-curvature point of the plasmonic inclusion. We provide partial theoretical explanation and link with the geometric structures of the Neumann-Poincaré (NP) eigenfunctions. The spectrum of the Neumann-Poincaré operator has received significant attentions in the literature. We show for the first time some intrinsic geometric structures of the Neumann-Poincaré eigenfunctions near high-curvature points.

Keywords. plasmonics, localization, geometrization, high-curvature, Neumann-Poincaré eigenfunctions

Mathematics Subject Classification (2010). 35R30, 35B30, 35Q60, 47G40

1. INTRODUCTION

There is considerable interest in the mathematical study of plasmon materials in recent years. Plasmon materials are a type of metamaterials that are artificially engineered to allow the presence of negative material parameters. We refer to [3, 4, 8, 21], [1, 2, 5, 12, 13, 14, 23, 28, 31, 32, 33, 34, 37, 38, 39, 40, 41, 42, 43] and [6, 7, 9, 10, 15, 25, 26, 29, 22, 24] and the references therein for the relevant studies in acoustics, electromagnetism and elasticity, respectively.

One peculiar and intriguing phenomenon associated with the plasmon materials is the so-called anomalous resonance [33]. Mathematically, the plasmon resonance is associated to the infinite dimensional kernel of a certain non-elliptic partial differential operator (PDO). In fact, the presence of negative material parameters breaks the ellipticity of the underlying partial differential equations (PDEs) that govern the various physical phenomena. Consequently, the non-elliptic PDO may possess a nontrivial kernel, which in turn may induce various resonance phenomena due to appropriate external excitations. In [1], applying techniques from the layer potential theory, the plasmon resonance is connected to the spectrum of the classical Neumann-Poincaré (NP) operator. Indeed, the aforementioned nontrivial kernel function of the underlying non-elliptic PDO can be represented as a single-layer potential. In order for plasmon resonance to occur, the density function of the above single-layer potential has to be an eigenfunction of the corresponding Neumann-Poincaré operator. In such a way, the plasmon parameters are also connected to the eigenvalues of the corresponding NP operator in a delicate way. The spectral properties of the NP operator were recently extensively investigated in the literature

[9, 15, 16, 17, 18, 19, 20, 27]. However, the corresponding studies are mainly concerned with the spectra of various NP operators in different geometric or physical setups. In this paper, we discover certain intrinsic geometric structures of the NP eigenfunctions. In fact, it is shown that the NP eigenfunctions as well as the associated single-layer potentials possess certain curvature-dependent behaviours locally near a boundary point. To our best knowledge, this is the first study in the literature on the intrinsic geometric properties of the NP eigenfunctions. The geometric results can be used to provide theoretical explanation of the localization and geometrization phenomenon in plasmon resonances, which is another novel and intriguing discovery in this paper, and also one of the major motivations for the investigation of the geometric structures of NP eigenfunctions.

The localization and geometrization in wave scattering were discovered and proposed in [11]. It states that if a certain wave scattering phenomenon occurs associated with a small object compared to the wavelength, then the similar phenomenon occurs for a “big” object but locally near a high-curvature boundary point. Noting that the global smallness condition means that the curvature is intrinsically high everywhere and hence the introduction of a local high-curvature condition is a natural one for the occurrence of the local scattering behaviour. In [11], the localization and geometrization phenomena were shown and justified in several time-harmonic scattering scenarios. In this paper, we show that the same principle actually holds for the plasmon resonances. In fact, in many of the existing studies on plasmon resonances, the quasi-static approximation has played a critical role where the plasmonic inclusion is of a size much smaller than the wavelength. There are also several studies that go beyond the quasi-static limit [33, 21, 27, 30, 36]. In [33], double negative materials are employed in the shell and in [36], in addition to the employment of double negative materials, a so-called double-complementary medium structure is incorporated into the construction of the plasmonic device. In [21], it is actually shown that resonance does not occur for the classical core-shell plasmonic structure without the quasistatic approximation as long as the core and shell are strictly convex. In [27, 30], in order for the plasmon resonances to occur beyond the quasi-static approximation, the corresponding plasmonic configuration has to be designed in a subtle and delicate way. Nevertheless, we show that for a plasmonic structure that is resonant in the quasi-static regime but non-resonant out of the quasi-static regime, the resonance always occurs locally near a high-curvature boundary point of the plasmonic inclusion. That is, the localization and geometrization phenomenon occurs for the plasmon resonances. This is mainly demonstrated by certain generic numerical examples. To seek a theoretical explanation, it naturally leads to the investigation of the geometric properties of the NP eigenfunctions as well as the associated single-layer potentials near a high-curvature boundary point.

The focus of our study is to present the novel and intriguing discoveries on the localization and geometrization in plasmon resonances as well as the intrinsic geometric structures of the NP eigenfunctions. We present our results mainly for the two-dimensional case though the extension to the three-dimensional case is also appealing. Moreover, in addition to the theoretical analysis, we resort to extensive numerical experiments in our study.

The rest of the paper is organized as follows. In Sections 2 and 3, we briefly discuss the plasmon resonances in the electrostatic and quasi-static cases. Section 4 presents the localization and geometrization phenomenon in the plasmon resonances. In Section 5, we investigate the geometric structures of the NP eigenfunctions. The paper is concluded in Section 6 with some relevant discussions.

2. PLASMON RESONANCE IN ELECTROSTATICS AND SPECTRAL SYSTEM OF NP OPERATOR

Let D be a bounded domain in \mathbb{R}^2 with a C^2 -smooth boundary ∂D and a connected complement $\mathbb{R}^2 \setminus \overline{D}$. Consider a dielectric medium configuration as follows,

$$\epsilon_\delta(x) = \begin{cases} \epsilon_c + i\delta, & x \in D, \\ 1, & x \in \mathbb{R}^2 \setminus \overline{D}, \end{cases} \quad (2.1)$$

where $\epsilon_c \in \mathbb{R}_-$ and $\delta \in \mathbb{R}_+$. Let $u \in H_{loc}^1(\mathbb{R}^2)$ signify the electric field associated with the medium configuration (2.1), and it satisfies the following PDE system,

$$\begin{cases} \nabla \cdot (\epsilon_\delta(x) \nabla u_\delta(x)) = f(x), & x \in \mathbb{R}^2, \\ u(x) = \mathcal{O}\left(\frac{1}{|x|}\right) & \text{as } |x| \rightarrow \infty, \end{cases} \quad (2.2)$$

where $f \in L^2(\mathbb{R}^2)$ is compactly supported in $\mathbb{R}^2 \setminus \overline{D}$ and

$$\int_{\mathbb{R}^2} f(x) \, dx = 0.$$

Associated with the electrostatic system (2.2), the configuration (ϵ_δ, f) is said to be *resonant* if there holds

$$\mathbf{E}_\delta(\epsilon_\delta, f) := \frac{\delta}{2} \int_D |\nabla u_\delta|^2 \, dx \rightarrow \infty \quad \text{as } \delta \rightarrow +0. \quad (2.3)$$

The condition (2.3) indicates that if plasmon resonance occurs, then highly oscillating behaviours are exhibited by the resonant field around the plasmon inclusion. Mathematically, the resonance is induced by the nontrivial kernel of the non-elliptic PDO (partial differential operator)

$$L_{\epsilon_0} u := \nabla \cdot (\epsilon_0 \nabla u), \quad (2.4)$$

where ϵ_0 is ϵ_δ with δ formally taken to be zero. The kernel of L_{ϵ_0} consists of nontrivial functions satisfying

$$u \in H_{loc}^1(\mathbb{R}^2); \quad L_{\epsilon_0} u(x) = 0, \quad x \in \mathbb{R}^2; \quad u(x) = \mathcal{O}\left(\frac{1}{|x|}\right) \text{ as } |x| \rightarrow \infty. \quad (2.5)$$

It is noted that ϵ_c is allowed to be negative, and hence the PDO L_{ϵ_0} is a non-elliptic operator. Therefore, if the plasmon constant ϵ_c is properly chosen, $\text{Ker}(L_{\epsilon_0})$ as defined in (2.5) can be nonempty, which in turn can induce resonance as described in (2.3) for a properly chosen external source f .

The connection to the spectral system of the Neumann-Poincaré operator can be described as follows. By the layer-potential theory, one seeks a solution to (2.5) of the following form

$$u(x) = S_{\partial D}[\varphi](x), \quad \varphi \in L_0^2(\partial D), \quad (2.6)$$

where $L_0^2(\partial D)$ is the space of square integrable functions with zero average on ∂D , and $S_{\partial D}[\varphi]$ is the singe-layer operator defined as

$$S_{\partial D}[\varphi](x) := \int_{\partial D} G(x-y) \varphi(y) \, ds(y), \quad x \in \mathbb{R}^2, \quad (2.7)$$

with

$$G(x) = \frac{1}{2\pi} \ln |x|, \quad (2.8)$$

being the fundamental solution of the Laplace operator in two dimensions. On the boundary ∂D , the single layer potential enjoys the following jump relationship

$$\partial_\nu S_{\partial D}[\varphi]|_\pm(x) = \left(\pm \frac{1}{2} + K_{\partial D}^*\right)[\varphi](x), \quad x \in \partial D, \quad (2.9)$$

where ∂_ν is the outward unit normal to ∂D and \pm indicate the limits to ∂D from outside and inside of D , respectively. In (2.9), the operator $K_{\partial D}^*$ is defined as

$$K_{\partial D}^*[\varphi](x) = \frac{1}{2\pi} \int_{\partial D} \frac{\langle x - y, \nu_x \rangle}{|x - y|^2} \varphi(y) ds(y), \quad x \in \partial D, \quad (2.10)$$

which is called the Neumann-Poincaré (NP) operator. By matching the transmission conditions across the boundary,

$$u|_- = u|_+, \quad \epsilon_c \partial_\nu u|_- = \partial_\nu u|_+, \quad (2.11)$$

and with the help of the jump formula (2.9), solving the system (2.5) is equivalent to solving the following problem

$$K_{\partial D}^*[\varphi](x) = \frac{\epsilon_c + 1}{2(\epsilon_c - 1)} \varphi(x), \quad x \in \partial D. \quad (2.12)$$

Clearly, according to our discussion made above, for the occurrence of the plasmon resonances, there are two critical conditions to be fulfilled from a spectral perspective associated with the NP operator defined in (2.10). First, the plasmon constant ϵ_c should be properly chosen such that the parameter $\lambda(\epsilon_c)$ defined as

$$\lambda(\epsilon_c) = \frac{\epsilon_c + 1}{2(\epsilon_c - 1)}, \quad (2.13)$$

belong to the spectrum of the NP operator K^* . Second, the single layer potential given in (2.6) associated with the NP eigenfunction φ according to (2.12) should exhibit certain highly oscillating behaviours around the plasmonic inclusion. The second condition naturally leads to the investigation of the structures of the NP eigenfunctions.

3. PLASMON RESONANCE FOR SMALL INCLUSIONS: QUASI-STATIC APPROXIMATION

In this section we consider the plasmon resonance for the wave scattering in the quasi-static regime. That is, the size of the plasmonic inclusion is much smaller than the underlying wavelength. To that end, we let Ω be a bounded domain in \mathbb{R}^2 with a C^2 -smooth boundary $\partial\Omega$ and a connected complement $\mathbb{R}^2 \setminus \overline{\Omega}$. Set $D = s\Omega$, where $s \in \mathbb{R}_+$ signifies a scaling parameter. Introduce the following plasmonic configuration,

$$\epsilon_{\mathcal{D},\delta}(x) = \begin{cases} \epsilon_c + i\delta, & x \in \mathcal{D}, \\ 1, & x \in \mathbb{R}^2 \setminus \overline{\mathcal{D}}, \end{cases} \quad (3.1)$$

where $\mathcal{D} = D$ or Ω . Associated with the medium configuration (3.1) in D , the wave scattering is governed by the following Helmholtz system

$$\begin{cases} \nabla \cdot (\epsilon_{D,\delta}(x) \nabla u_\delta(x)) + k^2 u_\delta(x) = f(x), & x \in \mathbb{R}^2, \\ \lim_{|x| \rightarrow \infty} |x|^{1/2} \left(\frac{x}{|x|} \cdot \nabla u_\delta - i k u_\delta \right) \rightarrow 0 & \text{as } |x| \rightarrow \infty, \end{cases} \quad (3.2)$$

where $k \in \mathbb{R}_+$ signifies a wavenumber and $f(x)$ is an external source that is compactly supported in $\mathbb{R}^2 \setminus \overline{D}$. The last limit in (3.2) is referred to as the Sommerfeld radiation condition. (3.2) describes the transverse electromagnetic wave scattering (cf. [27]).

Similar to the electrostatic case, if (2.3) occurs for the wave field in (3.2), the configuration is said to be resonant. In order to study the plasmon resonance associated with the Helmholtz system (3.2), by a straightforward scaling argument, the PDE system (3.2) can be transformed to

$$\nabla \cdot (\epsilon_{\Omega, \delta}(x) \nabla v_\delta(x)) + s^2 k^2 v_\delta(x) = \tilde{f}(x), \quad x \in \mathbb{R}^2, \quad (3.3)$$

where $v_\delta(x) = u_\delta(x/s)$ and $\tilde{f}(x) = f(x/s)$. In what follows, we introduce the following PDO,

$$(L_{\epsilon_{\Omega, 0}} + s^2 k^2)u := \nabla \cdot (\epsilon_{\Omega, 0} \nabla u) + s^2 k^2 u. \quad (3.4)$$

Similar to our discussion in the previous section, for the occurrence of the plasmon resonance, one needs to determine a nontrivial kernel of $L_{\epsilon_{\Omega, 0}} + s^2 k^2$ associated with a proper choice of ϵ_c . To that end, we introduce

$$S_{\partial D}^k[\varphi](x) := \int_{\partial D} G^k(x-y) \varphi(y) ds(y), \quad x \in \mathbb{R}^2, \quad (3.5)$$

$$(K_{\partial D}^k)^*[\varphi](x) := \int_{\partial D} \partial_{\nu_x} G^k(x-y) \varphi(y) ds(y) \quad x \in \partial D, \quad (3.6)$$

where

$$G^k(x) = -\frac{i}{4} H_0^1(k|x|),$$

with $H_0^1(t)$ zeroth-order Hankel function of the first kind. $S_{\partial D}^k$ and $(K_{\partial D}^k)^*$ are, respectively, the single-layer potential and the NP operator with a finite frequency $k \in \mathbb{R}_+$. According to our earlier discussion in Section 2, in order to study the plasmon resonance associated with (3.1), it suffices to investigate the nontrivial kernel of the PDO $L_{\epsilon_{\Omega, 0}} + s^2 k^2$. Similar to the electrostatic case, by using the layer-potential techniques, the study is reduced to analyzing the spectral system of the NP operator $(K_{\partial \Omega}^{sk})^*$ and the highly oscillating behaviours of the single-layer potentials $S_{\partial \Omega}^{sk}[\varphi]$ with φ being the NP eigenfunctions. Imposing the quasi-static condition,

$$s \cdot k \ll 1, \quad (3.7)$$

one has that

$$-\frac{i}{4} H_0^1(sk|x|) = \frac{1}{2\pi} \ln|x| + \tau + \sum_{n=1}^{\infty} (b_n \ln(sk|x|) + c_n) (sk|x|)^{2n}, \quad (3.8)$$

where

$$b_n = \frac{(-1)^n}{2\pi} \frac{1}{2^{2n}(n!)^2}, \quad c_n = -b_n \left(\gamma - \ln 2 - \frac{\pi i}{2} - \sum_{j=1}^n \frac{1}{j} \right), \quad (3.9)$$

$$\tau = \frac{1}{2\pi} (\ln(sk) + \gamma - \ln 2) - \frac{i}{4},$$

with γ the Euler constant. Therefore one can derive the following asymptotic expansions

$$S_{\partial \Omega}^{sk} = S_{\partial \Omega} + \tau \langle \cdot, 1 \rangle + (sk)^2 \ln(sk) \mathcal{R}^{sk}, \quad (3.10)$$

where \mathcal{R}^{sk} is a bounded operator from $L^2(\partial D)$ to $H^1(\partial D)$ and

$$(K_{\partial \Omega}^{sk})^* = K_{\partial \Omega}^* + (sk)^2 \ln(sk) \mathcal{Q}^{sk}, \quad (3.11)$$

where the operator \mathcal{Q}^{sk} is a bounded operator from $L^2(\partial \Omega)$ to itself. Hence, under the quasi-static approximation (3.7), the plasmon resonance for the Helmholtz system (3.2)

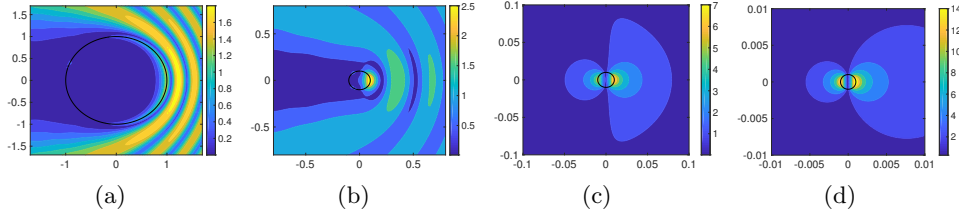


FIGURE 1. Moduli of the total wave fields of (3.2), (3.13) and (3.14) with (a). $s = 2$; (b). $s = 0.2$; (c). $s = 0.02$; (d). $s = 0.002$.

again relies on the spectral properties of the NP operator $K_{\partial\Omega}^*$ and the oscillating behaviours of the corresponding single-layer potentials that are same to the electrostatic case. In fact, it is rigorously justified in [4, 8] that under (3.7) and

$$s^2 |\ln s| \delta^{-1} \ll 1, \quad (3.12)$$

the Helmholtz system (3.2) is resonant for ϵ_c chosen from the resonant electrostatic case. Instead of discussing more theoretical details about the plasmon resonance within the quasi-static approximation, we next present several numerical examples for demonstration.

Consider a plasmon configuration of the form $\epsilon_{D,\delta}$ in (3.1) with

$$D = B_s(0), \quad \epsilon_c = -1, \quad \delta = 0.001, \quad (3.13)$$

where $B_s(0)$ is a central disc of radius $s \in \mathbb{R}_+$. The choice of $\epsilon_c = -1$ makes $\lambda(\epsilon_c)$ defined in (2.13) identically zero. It is noted that if D is a central disk, then 0 is actually the eigenvalue of K_D^* , and on the other hand, if D is an arbitrary domain with a C^2 boundary, K_D^* is a compact operator and 0 is an accumulation point of its eigenvalues. Hence, with $\epsilon_c = -1$, the first condition for the occurrence of the plasmon resonance is fulfilled. For the corresponding Helmholtz system (3.2), we choose

$$f = -\nabla \cdot (\epsilon_{D,\delta} \nabla u^i) - k^2 u^i, \quad u^i(x) = e^{ikx \cdot d}, \quad k = 10, \quad d = (-1, 0). \quad (3.14)$$

That means, the wave scattering is caused by an incident plane wave which plays the role of an external source. In Fig. 1, we plot the moduli of the total wave fields, namely $|u_\delta + u^i|$, against different parameters $s = 2$, $s = 0.2$, $s = 0.02$ and $s = 0.002$. The numerical results clearly show the critical role of the quasi-static approximation for the occurrence of the plasmon resonance. In fact, it can be seen that if the size of the plasmonic inclusion, namely $D = B_s(0)$, is not small enough compared to the wavelength, then resonance does not occur, and as s becomes smaller, both conditions (3.7) and (3.12) are fulfilled, then resonance occurs.

4. LOCALIZATION AND GEOMETRIZATION IN PLASMON RESONANCE

In this section, we consider the localization and geometrization for the plasmon resonance. We first present some numerical examples to illustrate this kind of peculiar phenomenon. Our numerical examples follow a similar setup as that specified in (3.13) and (3.14) with $s = 2$. According to our study in the previous section, we know that resonance does not occur. However, we pull out a part of the boundary of the plasmonic inclusion D to form a boundary point with a relatively high curvature; see Fig. 2 for the geometric setup. Similar to the numerical experiments in Fig. 1, we numerically plot the

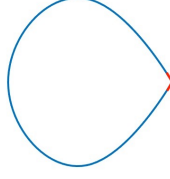


FIGURE 2. Geometry of the plasmonic inclusion D with a high-curvature boundary point.

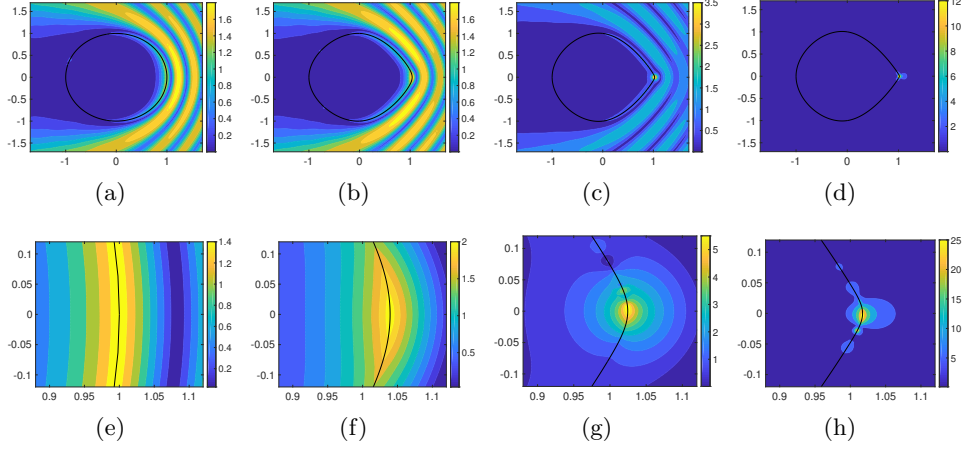


FIGURE 3. Localization and geometrization phenomenon in the plasmon resonance. The first row plots the moduli of the total fields with increasing curvatures at the same boundary point. The second row plots the moduli of the total fields locally around the high-curvature point.

total wave field associated to the plasmon inclusion as described above against the change of the curvature of the aforesaid boundary point; see Fig. 3. It can be readily seen that as the curvature of that boundary point increases to a certain degree, then resonance occurs locally around that high-curvature point. This is referred to as the localization and geometrization in the plasmon resonance. By localization, we mean that the resonance occurs only locally around a boundary point, whereas by geometrization, we mean that the global geometric smallness condition (3.7) can be replaced by a locally high-curvature condition. At this point, we would like to present our novel viewpoint about the plasmon resonance. That is, on the one hand, the plasmonic parameter is unquestionably a critical ingredient for the occurrence of resonance, but on the other hand, the quasi-static approximation, namely the smallness of the size of the plasmonic inclusion, is not the main cause for the resonance and instead, the high curvature is actually the main cause.

Next we try to provide a theoretical explanation of the localization and geometrization phenomenon in the plasmon resonance. According to our earlier discussion on the plasmon resonances, respectively, in the electrostatic and quasi-static cases, one needs to study the quantitative properties of the eigenfunctions of the NP operator $(K_{\partial D}^k)^*$ in (3.6) and the corresponding single-layer potential $S_{\partial D}^k[\varphi]$ in (3.5) locally around the high-curvature point of ∂D . To that end, let us consider a domain D as plotted in Fig. 2 and x_R be the vertex of the red part which possesses the largest curvature among all the boundary

points. Set

$$\Gamma_1 := \partial D \cap B_\rho(x_R), \quad \Gamma_2 := \partial D \setminus \Gamma_1, \quad (4.1)$$

where $\rho \in \mathbb{R}_+$ is sufficiently small. We have

Proposition 4.1. *Let ∂D , Γ_1 and Γ_2 be described above. There holds*

$$(K_{\partial D}^k)^*|_{\Gamma_1} = K_{\Gamma_1}^* + \mathcal{R}_{\Gamma_1, \rho} + \mathcal{T}, \quad (4.2)$$

where \mathcal{T} is a smooth operator on $L^2(\Gamma_1)$, and $\mathcal{R}_{\Gamma_1, \rho}$ is a bounded operator on $L^2(\Gamma_1)$ satisfying $\|\mathcal{R}_{\Gamma_1, \rho}\| = \mathcal{O}((\rho k)^2 \ln(\rho k))$.

Proof. From (4.1), one has that

$$(K_{\partial D}^k)^*|_{\Gamma_1} = (K_{\Gamma_1}^k)^*|_{\Gamma_1} + (K_{\Gamma_2}^k)^*|_{\Gamma_1},$$

where $(K_{\Gamma_2}^k)^*|_{\Gamma_1}$ is smooth operator on $L^2(\Gamma_1)$. Since $\Gamma_1 := \partial D \cap B_\rho(x_R)$ with $\rho \in \mathbb{R}_+$ sufficiently small, from the asymptotic expression for the NP operator in (3.11), one has by direct calculations that

$$(K_{\Gamma_1}^k)^*|_{\Gamma_1} = K_{\Gamma_1}^*|_{\Gamma_1} + \mathcal{R}_{\Gamma_1, \rho},$$

where $\mathcal{R}_{\Gamma_1, \rho}$ is a bounded operator on $L^2(\Gamma_1)$ satisfying

$$\|\mathcal{R}_{\Gamma_1, \rho}\| = \mathcal{O}((\rho k)^2 \ln(\rho k)).$$

The proof is complete. \square

Hence, by Proposition 4.1 and our earlier discussion on the plasmon resonance in the electrostatic and quasi-static cases, in order to understand the localization and geometrization phenomenon illustrated in Fig. 3, it is unobjectionable to say that one should investigate the spectral properties of the eigenfunctions of $K_{\partial D}^*$ locally near a high-curvature point. The rest of the paper is devoted to investigating the geometric structures of the NP eigenfunctions as well as the associated single-layer potentials near a high-curvature point. Finally, we mention that the geometrization with a high-curvature condition is a critical ingredient in our study. It is known that if ∂D is C^2 -smooth, then the corresponding NP operator is compact, and hence its spectrum consists only of eigenvalues. If the high-curvature point becomes a corner, then the corresponding NP operator possesses continuous spectra [16, 20, 17], which shall make the situation more complicated. Nevertheless, the NP operator may still possess eigenvalues in the corner domain case, and it is worth of future investigation on the corresponding NP eigenfunctions in such a case.

5. GEOMETRIC STRUCTURES OF NP EIGENFUNCTIONS

In this section, we consider the geometric structures of the eigenfunctions of the NP operator $K_{\partial D}^*$ as well as the corresponding single layer potential $S_{\partial D}[\varphi]$ near a high-curvature point of ∂D .

First, we present some basic results about the spectral structure of $K_{\partial D}^*$. Throughout the rest of the paper, we assume that ∂D is C^2 -smooth. As discussed earlier, $K_{\partial D}^*$ is a compact operator and its spectrum consists of at most countably many eigenvalues that can only accumulate at 0. We also know that (cf. [1])

$$\sigma(K_{\partial D}^*) \subset (-1/2, 1/2], \quad (5.1)$$

where and also in what follows, $\sigma(K_{\partial D}^*)$ signifies the spectrum of $K_{\partial D}^*$. There holds the following property

Lemma 5.1. *Suppose that $\lambda_0 = 1/2$ is an eigenvalue of $K_{\partial D}^*$ and $\psi_0 \in L^2(\partial D)$ is an eigenfunction, i.e. $K_{\partial D}^*[\psi_0] = 1/2\psi_0$. Then there holds*

$$S_{\partial D}[\psi_0](x) = C \in \mathbb{C}, \quad x \in D.$$

Proof. Set

$$u(x) = S_{\partial D}[\psi_0](x), \quad x \in \mathbb{R}^2.$$

By Green's formula one can show that

$$\int_D |\nabla u|^2 dx = \int_{\partial D} \frac{\partial u}{\partial \nu} \Big|_- \bar{u} ds = \int_{\partial D} (K^*[\psi_0] - 1/2\psi_0) \bar{u} ds = 0.$$

where ν signifies the exterior unit normal vector to ∂D . Hence, u must be constant on ∂D .

The proof is complete. \square

It is known that both $K_{\partial D}^*$ and $S_{\partial D}$ are pseudo-differential operators of order -1 (cf. [35]). Hence, if $\psi \in L^2(\partial D)$ is an eigenfunction satisfying $K_{\partial D}^*[\psi] = \lambda\psi$ for an eigenvalue $\lambda \in (-1/2, 1/2]$, it can be straightforwardly verify that $\psi \in C^{0,1}(\partial D)$. In fact, if ∂D is C^∞ -smooth, then $\psi \in C^\infty(\partial D)$.

Next, we investigate the geometric structures of the NP eigenfunctions. We start with the case that ∂D is an ellipse whose NP eigenfunctions can be explicitly calculated. For $x = (x_1, x_2) \in \mathbb{R}^2$, we introduce the following elliptic coordinates (ρ, ω) ,

$$x_1 = R_0 \cos \omega \cosh \rho, \quad x_2 = R_0 \sin \omega \sinh \rho, \quad \rho > 0, \quad 0 \leq \omega \leq 2\pi, \quad R_0 \in \mathbb{R}_+ \quad (5.2)$$

An elliptic domain D is defined by

$$D = \{(\rho, \omega); \rho \leq \rho_0, \quad 0 \leq \omega \leq 2\pi\}, \quad (5.3)$$

whose boundary is given by

$$\partial D = \{(\rho, \omega); \rho = \rho_0, \quad 0 \leq \omega \leq 2\pi\}. \quad (5.4)$$

In Fig. 4 we give a specific example with $R_0 = 1$ and $\rho_0 = 0.05$. In what follows, we set

$$\Xi := R_0 \sqrt{\sinh^2 \rho_0 + \sin^2 \omega}.$$

We have

Lemma 5.2 ([14]). *Let ∂D be an ellipse described in (5.2) and (5.4). There hold that*

$$K_{\partial D}^*[\phi_{1,n}] = a_n \phi_{1,n} \quad \text{and} \quad K_{\partial D}^*[\phi_{2,n}] = -a_n \phi_{2,n}, \quad n \geq 0,$$

where

$$\phi_{1,n} = \Xi^{-1} \cos n\omega, \quad \phi_{2,n} = \Xi^{-1} \sin n\omega \quad \text{and} \quad a_n = \frac{1}{2e^{2n\rho_0}}. \quad (5.5)$$

Moreover, associated with the eigenfunctions in (5.5), one has for $n \geq 1$ that

$$S_{\partial D}[\phi_{1,n}](x) = \begin{cases} -\frac{e^{n\rho} + e^{-n\rho}}{2ne^{n\rho_0}} \cos n\omega, & \rho \leq \rho_0, \\ -\frac{e^{n\rho_0} + e^{-n\rho_0}}{2ne^{n\rho}} \cos n\omega, & \rho > \rho_0, \end{cases}$$

and

$$S_{\partial D}[\phi_{2,n}](x) = \begin{cases} -\frac{e^{n\rho} + e^{-n\rho}}{2ne^{n\rho_0}} \sin n\omega, & \rho \leq \rho_0, \\ -\frac{e^{n\rho_0} + e^{-n\rho_0}}{2ne^{n\rho}} \sin n\omega, & \rho > \rho_0. \end{cases}$$

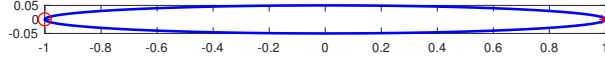


FIGURE 4. An ellipse defined by (5.2) and (5.4) with $R_0 = 1$ and $\rho_0 = 0.05$. The left and right vertices x_o and x_* , respectively, on the semi-major axis are the high-curvature points.

With the explicit forms of the NP eigenfunctions and the associated single-layer potentials, we are in a position to investigate their geometric structures. Before that, we first note that for an ellipse defined by (5.2) and (5.4), the corresponding curvature at a boundary point $(\rho_0, \omega) \in \partial D$ can be directly calculated to be

$$\kappa(\omega) = \frac{\cosh \rho_0 \sinh \rho_0}{R_0 (\sinh^2 \rho_0 + \sin^2 \omega)^{3/2}}. \quad (5.6)$$

Hence, the largest curvature is attainable at the two vertices with $\omega = \pi$ and $\omega = 0$ respectively on the semi-major axis, denoted as x_o and x_* in what follows; see Fig. 4 for an illustration. Henceforth, the points on ∂D that attain the largest curvature are referred to as the high-curvature points. By (5.6), the largest curvature is given by

$$\kappa_{\max} := \frac{\cosh \rho_0}{R_0 \sinh^2 \rho_0}. \quad (5.7)$$

It is noted that for a fixed R_0 , the curvature κ_{\max} increases as ρ_0 decreases and actually one has that $\kappa_{\max} \rightarrow \infty$ as $\rho_0 \rightarrow +0$. In what follows, we shall also need the conormal derivative of a function $\psi(x)$ defined over ∂D . Let ∂D be parametrized as $x(s)$, and then the conormal derivative of $\psi(x)$ is defined as

$$d\psi = \psi'(x) \cdot \frac{x'(s)}{|x'(s)|} = \frac{d}{ds} \psi(x(s)) \frac{1}{|x'(s)|}.$$

Proposition 5.3. *Let ∂D be an ellipse described in (5.2) and (5.4), and let $\phi_{1,n}$ and $\phi_{2,n}$ be the NP eigenfunctions derived in Lemma 5.2 for $K_{\partial D}^*$ with $n \geq 1$. Then one has*

- (1) $\phi_{1,n}(x)$ achieves its maximum absolute value on ∂D at x_o and x_* ,

$$|\phi_{1,n}(x_o)| = |\phi_{1,n}(x_*)| = \tau_{\max}, \quad \tau_{\max} := \frac{1}{R \sinh \rho_0}, \quad (5.8)$$

and there holds the following asymptotic relationship as $\kappa_{\max} \rightarrow +\infty$, or equivalently $\rho_0 \rightarrow +0$,

$$\tau_{\max} \sim \alpha \kappa_{\max}^p, \quad p = 1/2, \quad \alpha \in \mathbb{R}_+. \quad (5.9)$$

- (2) $d\phi_{2,n}$ achieves its maximum absolute value on ∂D at x_o and x_* ,

$$|d\phi_{2,n}(x_o)| = |d\phi_{2,n}(x_*)| = \tau'_{\max}, \quad \tau'_{\max} := \frac{n}{R_0 \sinh^2 \rho_0}, \quad (5.10)$$

and moreover there holds

$$\tau'_{\max} \rightarrow \infty \quad \text{as} \quad \kappa_{\max} \rightarrow \infty. \quad (5.11)$$

- (3) $S_{\partial D}[\phi_{1,n}]$ and $dS_{\partial D}[\phi_{2,n}]$, respectively, achieve their maximum absolute values at x_o and x_* .

Proof. With the explicit forms of solutions in Lemma 5.2, the proposition can be verified by straightforward though a bit tedious calculations. \square

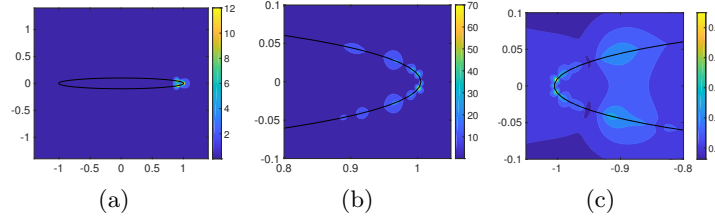


FIGURE 5. Localization and geometrization phenomenon in the plasmon resonance associated with an elliptical inclusion. (a). Modulus of the total wave field around the whole plasmonic inclusion; (b), (c). Modulus of the total wave field around x_* and x_o , respectively.

In Proposition 5.3, we did not consider the case with $n = 0$ due to Lemma 5.1. Clearly, the properties in Proposition 5.3 can be used to explain the localization and geometrization phenomenon discovered in Section 4, at least for the elliptic geometry case. In fact, we perform the numerical experiment in Fig. 3 again, but with the plasmonic inclusion ∂D in Fig. 2 replaced by an ellipse in Fig. 4. The loss parameter δ is set to be 0.0001. The total wave field is plotted in Fig. 5. Clearly, strong resonant behaviours are observed locally around the two high-curvature points x_o and x_* . It is remarked that the incident plane wave propagates from the left to the right and the vertex x_o is located in the shadow region. Hence, the resonant behaviour around x_* is stronger than that around x_o .

We believe those beautiful geometric structures in Proposition 5.3 for the NP eigenfunctions and the associated single-layer potentials hold for more general geometries. However, dealing with the general geometries, it is unpractical to derive the explicit forms of the NP eigenfunctions and the associated single-layer potentials. We have conducted extensive numerical experiments within general geometries and indeed the NP eigenfunctions exhibit certain intrinsic geometric structures near a boundary point with a high curvature. Before presenting our discoveries, we first introduce the notion of a symmetric domain. Consider a star-shaped domain D whose boundary ∂D is parametrized as follows,

$$\partial D = r(\theta)\hat{x}(\theta), \quad \hat{x}(\theta) = (\cos \theta, \sin \theta), \quad \theta \in [0, 2\pi), \quad (5.12)$$

where $r \geq 0$ is the radial function. If there exists $n \in \mathbb{N}$ such that

$$r(\theta) = r(\theta + 2\pi/n), \quad (5.13)$$

the domain D is said to be n -symmetric. Clearly, the domain in Fig. 2 is 1-symmetric and the domain in Fig. 4 is 2-symmetric. An n -symmetric domain possesses n high-curvature points.

The major numerical discoveries can be summarized as follows:

- (1) Suppose D is convex with ∂D satisfying (5.12), and $\lambda \in \sigma(K_{\partial D}^*)$. If λ is positive and simple, then the absolute values of both its eigenfunction and the corresponding single-layer potential blow up at the high-curvature point(s) on ∂D as the corresponding curvature goes to infinity; whereas if λ is positive and multiple, then there exists at least one of the eigenfunctions such that the absolute values of both the eigenfunction and the associated single-layer potential blow up at the high-curvature point(s) on ∂D as the corresponding curvature goes to infinity. If λ is negative, then similar conclusions hold at the high-curvature

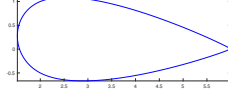


FIGURE 6. A convex 1-symmetric domain.

point(s), but for the conormal derivatives of the eigenfunction and the associated single-layer potential.

- (2) Suppose D is concave at the high-curvature point(s) with ∂D satisfying (5.12), and $\lambda \in \sigma(K_{\partial D}^*)$. If λ is negative and simple, then the absolute values of both its eigenfunction and the associated single-layer potential blow up at the high-curvature point(s) on ∂D as the corresponding curvature goes to infinity; whereas if λ is positive and multiple, then there exists at one of the eigenfunctions such that the absolute values of both the eigenfunction and the associated single-layer potential blow up at the high-curvature point(s) on ∂D as the corresponding curvature goes to infinity. If λ is positive, then similar conclusions hold at the high-curvature point(s), but for the conormal derivatives of the eigenfunction and the associated single-layer potential.
- (3) If D is non-symmetric, then the NP eigenfunction or its conormal derivative as well as the corresponding single-layer potential may still possess the blow-up behaviour at a high-curvature point, but the situation is more complicated, and there is no definite conclusion about it.

5.1. Numerical method. We first introduce the numerical method used to calculate the spectral system of the NP operator defined in (2.10) and the corresponding single layer potential. Assume that the boundary of D , i.e. ∂D , is parameterized by $r(t)$, $t \in (0, 2\pi)$. Then the NP operator can be expressed as follows

$$K^*[\varphi](x) = \frac{1}{2\pi} \int_0^{2\pi} \frac{\langle r(s) - r(t), \nu_s \rangle}{|r(s) - r(t)|^2} \varphi(r(t)) |r'(t)| dt. \quad (5.14)$$

To numerically calculate this integral, we first discretize the integral line into n panels and on each panel, we utilize the 16-point Gauss-Legendre quadrature formula. We point out that from the expression in (5.14), there is the singularity when $t = s$, namely $y = x$. However, noting that $r(t) \in C^2(\partial D)$, the singularity can be removed by using the following identity,

$$\lim_{t \rightarrow s} \frac{\langle r(s) - r(t), \nu_s \rangle}{|r(s) - r(t)|^2} = -\frac{\langle r''(s), \nu_s \rangle}{2|r'(s)|^2},$$

where ν_s signifies the exterior unit normal vector to ∂D at $r(s)$.

5.2. A convex 1-symmetric domain. Let us first consider a domain D with one high-curvature point, denoted as x_* , as shown in Fig. 6, and the largest curvature is 500. The first seven largest NP eigenvalues (in terms of the absolute value) are numerically found to be

$$\begin{aligned} \lambda_0 &= 0.5, \quad \lambda_1 = 0.2575, \quad \lambda_2 = -0.2575, \quad \lambda_3 = 0.1365, \\ \lambda_4 &= -0.1365, \quad \lambda_5 = 0.0685, \quad \lambda_6 = -0.0685. \end{aligned} \quad (5.15)$$

It is remarked that all of the eigenvalues are simple.

Fig. 7 plots the eigenfunctions as well as the associated single-layer potentials, respectively, for the positive eigenvalues $\lambda_1 = 0.2575$ and $\lambda_3 = 0.1365$. The numerical results

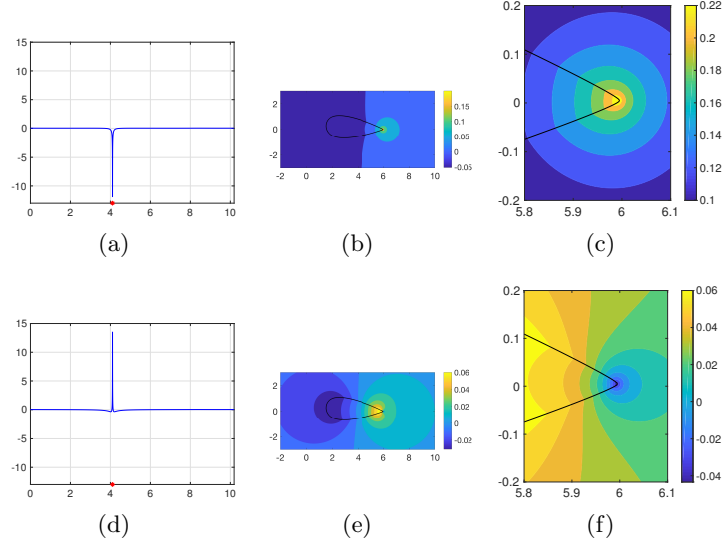


FIGURE 7. (a). Plotting of the eigenfunction for $\lambda_1 = 0.2575$ with respect to the arc length; (b). The associated single-layer potential for $\lambda_1 = 0.2575$; (c). The single-layer potential around the high-curvature point; (d), (e), (f). The corresponding items for $\lambda_3 = 0.1365$.

clearly support our assertion about the NP eigenfunctions associated to simple positive eigenvalues.

Fig. 8 plots the eigenfunctions as well as the corresponding conormal derivatives and single-layer potentials for the negative eigenvalues $\lambda_2 = -0.2575$ and $\lambda_4 = -0.1365$, respectively. The numerical results clearly support our assertion about the NP eigenfunctions associated to simple negative eigenvalues.

Fig. 9 plots the eigenfunctions with respect to arc length for the eigenvalues $\lambda_1 = 0.2575$ and $\lambda_2 = -0.2575$ with different maximum curvature 500, 1000 and 1500.

We also numerically investigate the blow-up rate of the eigenfunction or its conormal derivative at a high-curvature point and plot the logarithm of the absolute value of the eigenfunctions at the high-curvature point for the positive eigenvalues λ_1 , λ_3 and λ_5 , and the logarithm of the absolute value of the derivative of the eigenfunctions at the high-curvature point for the negative eigenvalues λ_2 , λ_4 and λ_6 with respect to different curvature in Fig. 10. We find that they always follow the following rule

$$\psi_{\max} \sim a\kappa_{\max}^p \quad \text{as } \kappa_{\max} \rightarrow +\infty, \quad (5.16)$$

where $\alpha, p \in \mathbb{R}_+$ and ψ_{\max} signifies the absolute value at the high-curvature point for the eigenfunction if the corresponding eigenvalue is positive, and for the conormal derivative of the eigenfunction if the eigenvalue is negative. In fact, by increasing the curvature at the point x_* and using a standard regression, we can find the blow-up rates for different eigenvalues in (5.15). The parameters from the regression are listed in Table 1.

5.3. A convex 3-symmetric domain. In this subsection, we consider a convex 3-symmetric domain as shown in Fig. 11, which possesses three high-curvature points that are denoted by x_* , x_Δ and x_o as shown in Fig. 11. The largest curvature is

$$\kappa_{x_*} = \kappa_{x_\Delta} = \kappa_{x_o} = 500. \quad (5.17)$$

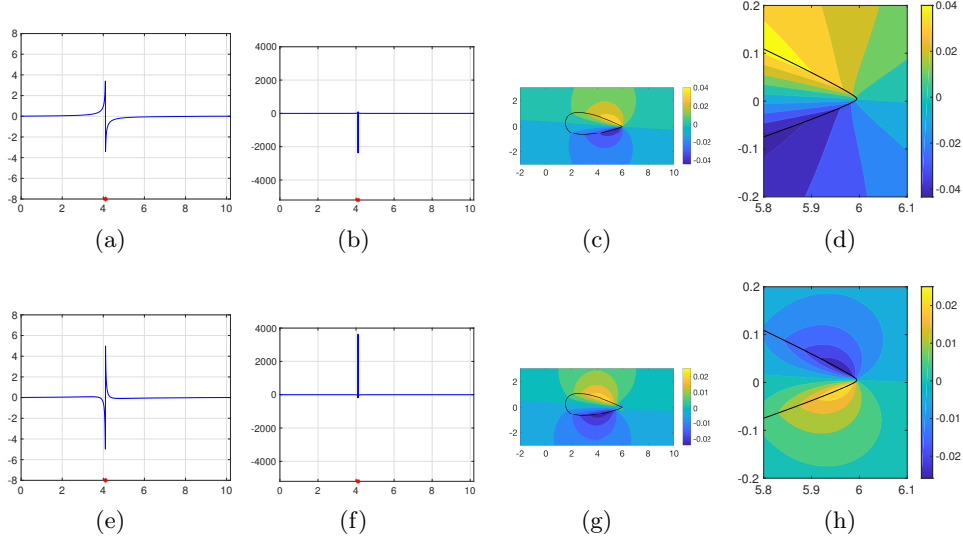


FIGURE 8. (a), (b). Plotting of the eigenfunction and its conormal derivative for $\lambda_2 = -0.2575$; (c), (d). The associated single-layer potential for $\lambda_2 = -0.2575$; (e), (f), (g), (h). The corresponding items for the negative eigenvalues $\lambda_4 = -0.1365$.

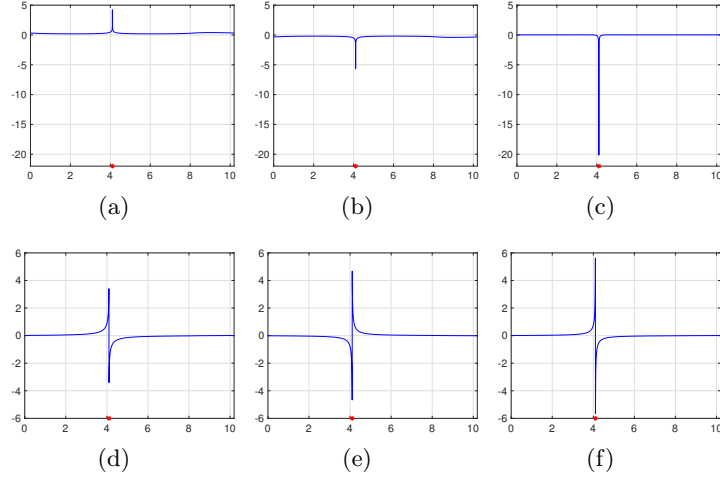


FIGURE 9. (a), (b), (c). Plotting the eigenfunctions for the positive eigenvalues $\lambda_1 = 0.2575$ with different maximum curvature 500, 1000 and 1500. (d), (e), (f). The corresponding items for the negative eigenvalue $\lambda_2 = -0.2575$.

The first seven largest eigenvalues (in terms of the absolute value) are numerically found to be

$$\begin{aligned}
 \lambda_0 &= 0.5, \quad \lambda_1 = \lambda_2 = 0.2850, \quad \lambda_3 = \lambda_4 = -0.2850, \quad \lambda_5 = 0.2583, \quad \lambda_6 = -0.2583, \\
 \lambda_7 &= \lambda_8 = 0.1906, \quad \lambda_9 = \lambda_{10} = -0.1906, \quad \lambda_{11} = 0.1568, \quad \lambda_{12} = -0.1568, \\
 \lambda_{13} &= \lambda_{14} = 0.1111, \quad \lambda_{15} = \lambda_{16} = -0.1111, \quad \lambda_{17} = 0.0875, \quad \lambda_{18} = -0.0875.
 \end{aligned} \tag{5.18}$$

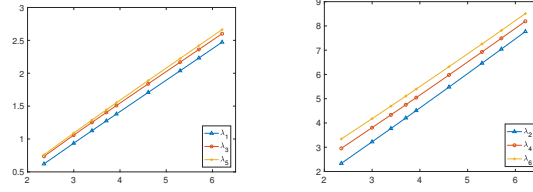


FIGURE 10. The left one plots logarithm of the eigenfunction at the high-curvature point for the positive eigenvalues λ_1 , λ_3 and λ_5 , and the right one plots logarithm of the derivative of the eigenfunction at the high-curvature point for the simple negative eigenvalues λ_2 , λ_4 and λ_6 with respect to different curvature.

(a)				(b)			
	λ_1	λ_3	λ_5		λ_2	λ_4	λ_6
p	0.4793	0.4824	0.4925	p	1.4108	1.3602	1.3423
$\ln(\alpha)$	-0.5022	-0.3886	-0.3867	$\ln(\alpha)$	-1.0102	-0.2763	-0.1483

TABLE 1. The parameters of the form (5.16) from the regression associated with the eigenvalues in (5.15): (a) $\lambda_j, j = 1, 3, 5$; (b) $\lambda_j, j = 2, 4, 6$.

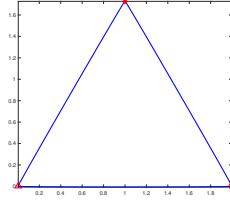


FIGURE 11. A convex 3-symmetric domain.

Compared to the study in the previous subsection, there are multiple NP eigenvalues occurring for the 3-symmetric domain. Hence, we can verify our assertion about the NP eigenfunction associated to a multiple NP eigenvalue. In the following, we first show the case for the simple eigenvalue and then the case for the multiple eigenvalue.

Fig. 12 plots the eigenfunctions as well as the associated single-layer potentials, respectively, for the positive eigenvalues $\lambda_5 = 0.2583$. The numerical results clearly support our assertion about the NP eigenfunctions associated to simple positive eigenvalues.

Fig. 13 plots the eigenfunctions as well as the corresponding conormal derivatives and single-layer potentials for the negative eigenvalues $\lambda_6 = -0.2583$. The numerical results clearly support our assertion about the NP eigenfunctions associated to simple negative eigenvalues.

Fig. 14 plots the eigenfunctions with respect to arc length for the eigenvalues $\lambda_5 = 0.2583$ and $\lambda_6 = -0.2583$ with different maximum curvature 500, 1000 and 1500.

We next investigate the blow-up rate of the NP eigenfunction or its conormal derivative with respect to the curvature. Therefore we plot the logarithm of the absolute value of the eigenfunctions at the high-curvature point for the positive eigenvalues λ_5 , λ_{11} and λ_{17} , and the logarithm of the absolute value of the derivative of the eigenfunctions at the

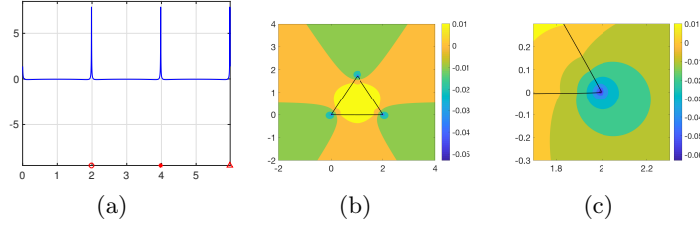


FIGURE 12. (a). Plotting of the eigenfunction for $\lambda_5 = 0.2583$ with respect to the arc length; (b). The associated single-layer potential for $\lambda_5 = 0.2583$; (c). The single-layer potential around the high-curvature point;

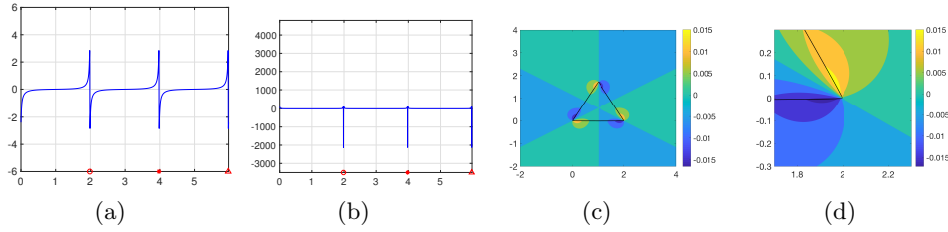


FIGURE 13. (a), (b). Plotting of the eigenfunction and its conormal derivative for $\lambda_6 = -0.2583$; (c), (d). The associated single-layer potential for $\lambda_6 = -0.2583$.

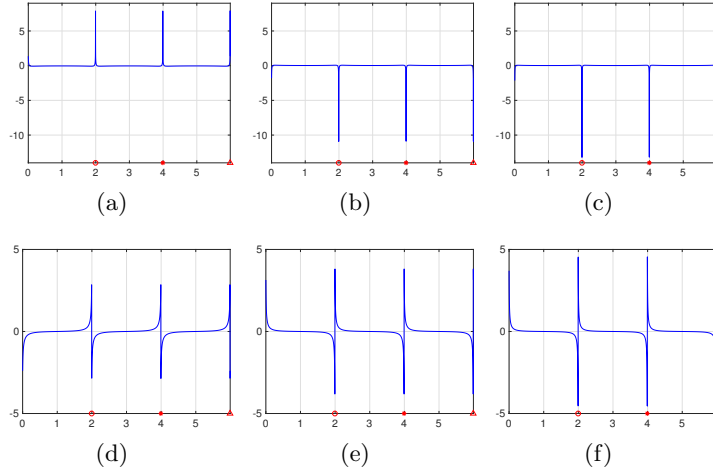


FIGURE 14. (a), (b), (c). Plotting the eigenfunctions for the positive eigenvalues $\lambda_5 = 0.2583$ with different maximum curvature 500, 1000 and 1500. (d), (e), (f). The corresponding items for the negative eigenvalue $\lambda_6 = -0.2583$.

high-curvature point for the negative eigenvalues λ_6 , λ_{12} and λ_{18} with respect to different curvature in Fig. 15. It turns out that blow-up rate also follows the rule in (5.16). By

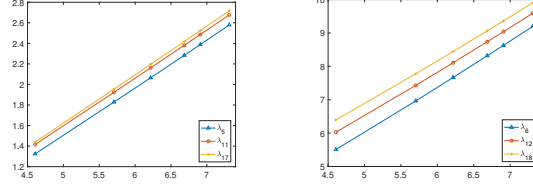


FIGURE 15. The left one plots logarithm of the eigenfunction at the high-curvature point for the simple positive eigenvalues λ_5 , λ_{11} and λ_{17} , and the right one plots logarithm of the derivative of the eigenfunction at the high-curvature point for the simple negative eigenvalues λ_6 , λ_{12} and λ_{18} with respect to different curvature.

(a)				(b)			
	λ_5	λ_{11}	λ_{17}		λ_6	λ_{12}	λ_{18}
p	0.4632	0.4659	0.720	p	1.3641	1.3170	1.2963
$\ln(a)$	-0.8117	-0.7322	-0.7360	$\ln(a)$	-0.7958	-0.0611	0.4046

TABLE 2. The coefficients of the regression; (a) $\lambda_j, j = 5, 11, 17$; (b) $\lambda_j, j = 6, 12, 18$.

regression, we numerically determine the corresponding parameters for those different eigenvalues in (5.18), and they are listed in Table 2.

Next we show the corresponding properties for the multiple eigenvalues. Fig. 16 plots the two linearly independent eigenfunctions associated with the multiple eigenvalue $\lambda_1 = \lambda_2 = 0.2850$, as well as the corresponding single-layer potentials. The numerical results clearly support our assertion about the NP eigenfunctions associated with multiple positive NP eigenvalues.

Fig. 17 plots the two linearly independent eigenfunctions associated with the multiple eigenvalue $\lambda_3 = \lambda_4 = -0.2850$, as well as the corresponding conormal derivatives and the corresponding single-layer potentials. The numerical results clearly support our assertion about the NP eigenfunctions associated with multiple negative NP eigenvalues.

5.4. A convex 4-symmetric domain. In this subsection, we consider a convex 4-symmetric domain as shown in Fig. 18, which possesses four high-curvature points that are denoted by x_\times , x_o , x_* and x_Δ as shown in Fig. 18. The largest curvature is

$$\kappa_{x_\times} = \kappa_{x_o} = \kappa_{x_*} = \kappa_{x_\Delta} = 500. \quad (5.19)$$

The first eleven largest eigenvalues (in terms of the absolute value) are numerically found to be

$$\begin{aligned} \lambda_0 = 0.5, \quad \lambda_1 = 0.2183, \quad \lambda_2 = -0.2183, \quad \lambda_3 = \lambda_4 = 0.2113, \quad \lambda_5 = \lambda_6 = -0.2113, \\ \lambda_7 = 0.1934, \quad \lambda_8 = -0.1934, \quad \lambda_9 = 0.1313, \quad \lambda_{10} = -0.1313. \end{aligned} \quad (5.20)$$

There are multiple NP eigenvalues occurring for the 4-symmetric domain. Hence, we can verify our assertion about the NP eigenfunction associated to a multiple NP eigenvalue. In the following, we first show the case for the simple eigenvalue and then the case for the multiple eigenvalue.

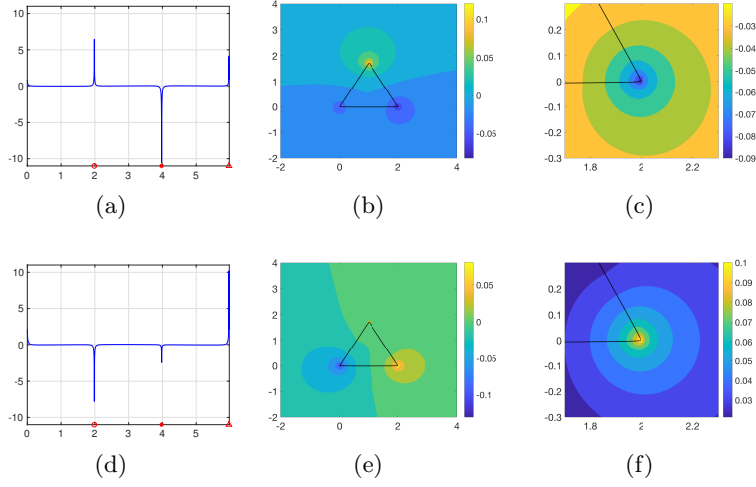


FIGURE 16. (a), (b), (c). The first eigenfunction associated with $\lambda_1 = \lambda_2 = 0.2850$ as well as the corresponding single-layer potential; (d), (e), (f). The second eigenfunction associated with $\lambda_1 = \lambda_2 = 0.2850$ as well as the corresponding single-layer potential.

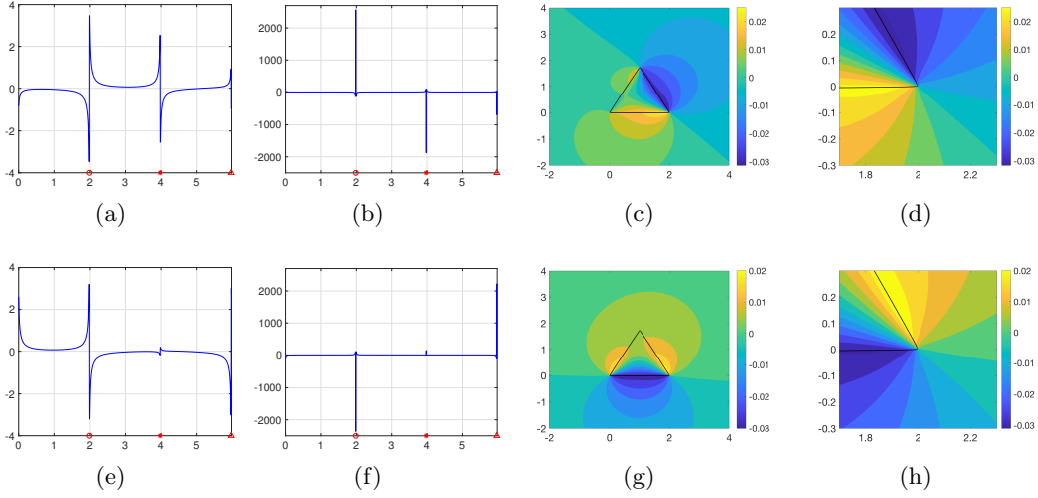


FIGURE 17. (a), (b), (c), (d). The first eigenfunction associated with $\lambda_3 = \lambda_4 = -0.28500$ as well as the corresponding conormal derivatives and the corresponding single-layer potential; (e), (f), (g), (h). The second eigenfunction associated with $\lambda_3 = \lambda_4 = -0.2850$ as well as the corresponding conormal derivatives and the corresponding single-layer potential.

Fig. 19 plots the eigenfunctions as well as the associated single-layer potentials, respectively, for the positive eigenvalues $\lambda_1 = 0.2183$. The numerical results clearly support our assertion about the NP eigenfunctions associated to simple positive eigenvalues.

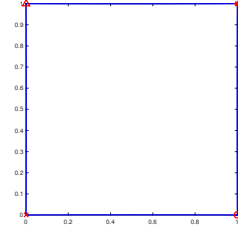


FIGURE 18. The boundary with four high-curvature points.

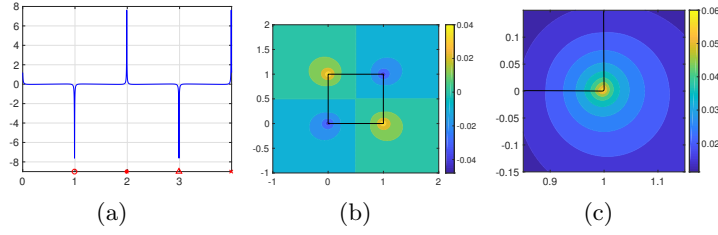
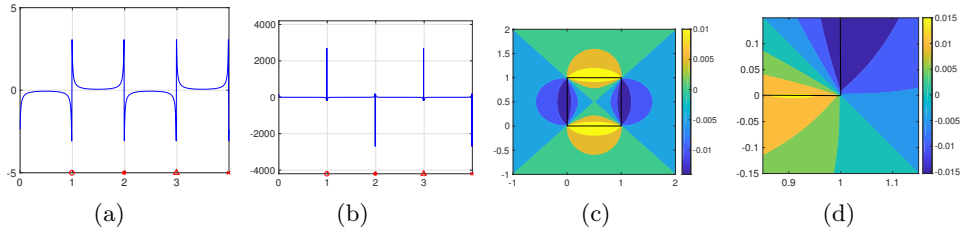
FIGURE 19. (a). Plotting of the eigenfunction for $\lambda_1 = 0.2183$ with respect to the arc length; (b). The associated single-layer potential for $\lambda_1 = 0.2183$; (c). The single-layer potential around the high-curvature point.FIGURE 20. (a), (b). Plotting of the eigenfunction and its conormal derivative for $\lambda_2 = -0.2183$; (c), (d). The associated single-layer potential for $\lambda_2 = -0.2183$.

Fig. 20 plots the eigenfunctions as well as the corresponding conormal derivatives and single-layer potentials for the negative eigenvalues $\lambda_2 = -0.2183$. The numerical results clearly support our assertion about the NP eigenfunctions associated to simple negative eigenvalues.

Fig. 21 plots the eigenfunctions with respect to arc length for the eigenvalues $\lambda_1 = 0.2183$ and $\lambda_2 = -0.2183$ with different maximum curvature 500, 1000 and 1500.

We next investigate the blow-up rate of the NP eigenfunction or its conormal derivative with respect to the curvature. Therefore we plot the logarithm of the absolute value of the eigenfunctions at the high-curvature point for the positive eigenvalues λ_1 , λ_7 and λ_9 , and the logarithm of the absolute value of the conormal derivative of the eigenfunctions at the high-curvature point for the simple negative eigenvalues λ_2 , λ_8 and λ_{10} with respect to different curvature in Fig. 22. It turns out that blow-up rate also follows the rule in

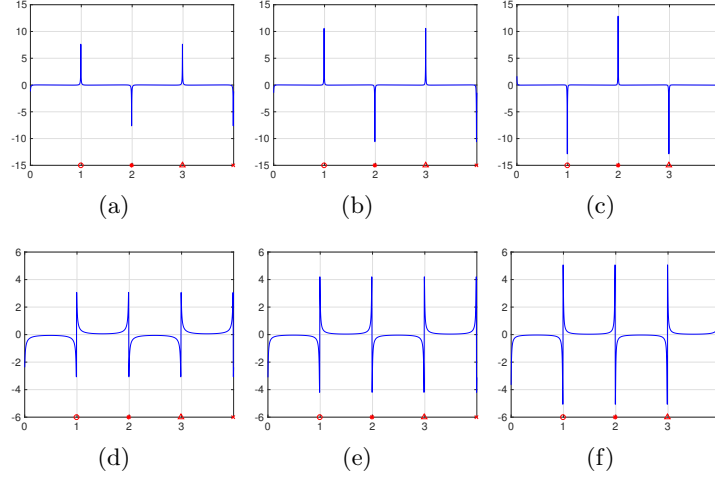


FIGURE 21. (a), (b), (c). Plotting the eigenfunctions for the positive eigenvalues $\lambda_1 = 0.2183$ with different maximum curvature 500, 1000 and 1500. (d), (e), (f). The corresponding items for the negative eigenvalue $\lambda_2 = -0.2183$.

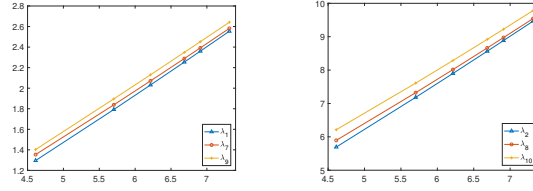


FIGURE 22. The logarithm of the eigenfunction at the high-curvature point x_o for the positive eigenvalues λ_1 , λ_7 and λ_9 , and the negative eigenvalues λ_2 , λ_8 and λ_{10} with respect to different curvature.

(a)				(b)			
	λ_1	λ_7	λ_9		λ_2	λ_8	λ_{10}
p	0.4657	0.4544	0.4584	p	1.3951	1.3492	1.3198
$\ln(a)$	-0.8579	-0.7477	-0.7147	$\ln(a)$	-0.7562	-0.3501	0.1044

TABLE 3. The coefficients of the regression; (a) $\lambda_j, j = 1, 7, 9$; (b) $\lambda_j, j = 2, 8, 10$.

(5.16). By regression, we numerically determine the corresponding parameters for those different eigenvalues in (5.20), and they are listed in Table 3.

5.5. A concave 1-symmetric domain. In this subsection, we consider a concave 1-symmetric domain as shown in Fig. 23, which possesses one high-curvature points that are denoted by x_* and x_o . The largest curvature is

$$\kappa_{\max} = \kappa_{x_*} = \kappa_{x_o} = 500. \quad (5.21)$$

The first five largest NP eigenvalues (in terms of the absolute value) are

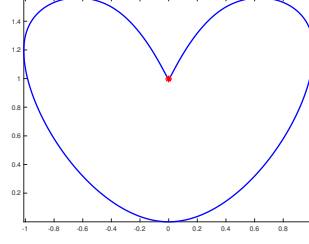
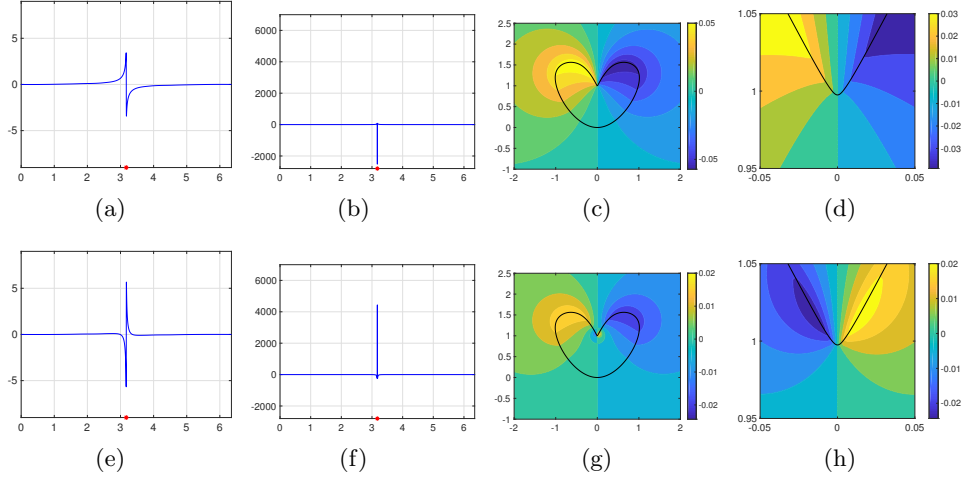


FIGURE 23. the boundary with one high-curvature point

FIGURE 24. (a), (b), (c), (d). The eigenfunction, its conormal derivative, and the corresponding single-layer potential associated with $\lambda_1 = 0.3310$; (e), (f), (g), (h). The corresponding items associated with $\lambda_3 = 0.2142$.

$$\begin{aligned} \lambda_0 = 0.5, \quad \lambda_1 = 0.3310, \quad \lambda_2 = -0.3310, \quad \lambda_3 = 0.2142, \\ \lambda_4 = -0.2142, \quad \lambda_5 = 0.1262 \quad \lambda_6 = -0.1262. \end{aligned} \quad (5.22)$$

Fig. 24 plots the eigenfunctions, their conormal derivatives and the associated single-layer potentials, respectively, associated with the eigenvalues $\lambda_1 = 0.3310$ and $\lambda_3 = 0.2142$. The numerical results clearly support our earlier assertion about the NP eigenfunctions associated with simple positive eigenvalues.

Fig. 25 plots the eigenfunctions, their conormal derivatives and the associated single-layer potentials, respectively, associated with the eigenvalues $\lambda_2 = -0.3310$ and $\lambda_4 = -0.2142$. The numerical results clearly support our earlier assertion about the NP eigenfunctions associated with simple negative eigenvalues.

Fig. 26 plots the eigenfunctions with respect to arc length for the eigenvalues $\lambda_1 = 0.3310$ and $\lambda_2 = -0.3310$ with different maximum curvature 500, 1000 and 1500.

We next investigate the blow-up rate of the NP eigenfunction or its conormal derivative with respect to the curvature. Therefore we plot the logarithm of the derivative of the absolute value of the eigenfunctions at the high-curvature point for the positive eigenvalues λ_1 , λ_3 and λ_5 , and the logarithm of the absolute value of the eigenfunctions at the high-curvature point for the negative eigenvalues λ_2 , λ_4 and λ_6 with respect to different curvature in Fig. 27. It turns out that blow-up rate also follows the rule in

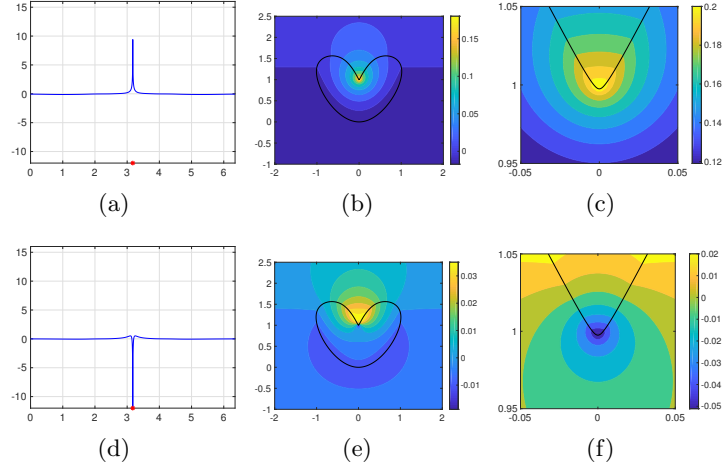


FIGURE 25. (a), (b), (c). The eigenfunction, its conormal derivative, and the corresponding single-layer potential associated with $\lambda_2 = -0.3310$; (d), (e), (f). The corresponding items associated with $\lambda_4 = -0.2142$.

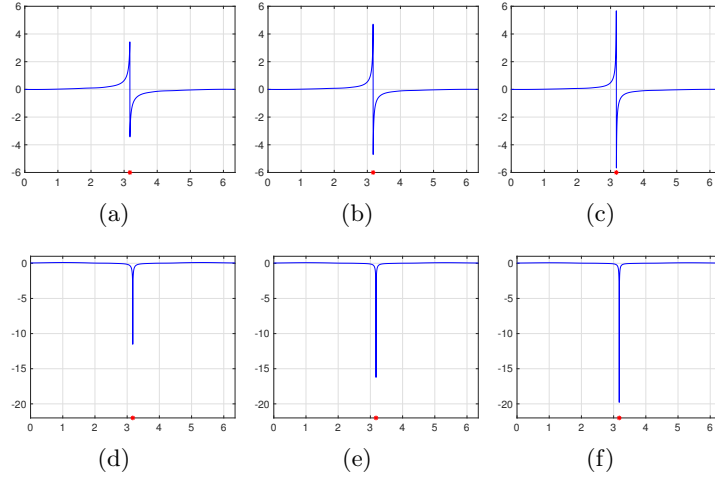


FIGURE 26. (a), (b), (c). Plotting the eigenfunctions for the positive eigenvalues $\lambda_1 = 0.3310$ with different maximum curvature 500, 1000 and 1500. (d), (e), (f). The corresponding items for the negative eigenvalue $\lambda_2 = -0.3310$.

(5.16). By regression, we numerically determine the corresponding parameters for those different eigenvalues in (5.22), and they are listed in Table 4.

5.6. A concave 2-symmetric domain. In this subsection, we consider a concave 2-symmetric domain as shown in Fig. 28, which possesses two high-curvature points that are denoted by x_* and x_o . The largest curvature is

$$\kappa_{\max} = \kappa_{x_*} = 500. \quad (5.23)$$

The first five largest NP eigenvalues (in terms of the absolute value) are

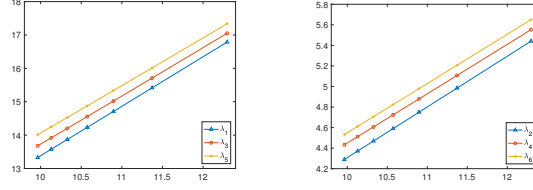


FIGURE 27. The logarithm of the absolute value of the conormal derivative of the eigenfunction at the high-curvature point for the positive eigenvalues λ_1 , λ_3 and λ_5 and the logarithm of the absolute value of the eigenfunction at the high-curvature point is the largest for the negative eigenvalues λ_2 , λ_4 and λ_6 with respect to different curvature.

(a)				(b)			
	λ_1	λ_3	λ_5		λ_2	λ_4	λ_6
p	1.4814	1.4454	1.4253	p	0.4934	0.4803	0.4795
$\ln(a)$	-1.4367	-0.7261	-0.1924	$\ln(a)$	-0.6267	-0.3545	-0.2455

TABLE 4. The coefficients of the regression; (a) $\lambda_j, j = 1, 3, 5$; (b) $\lambda_j, j = 2, 4, 6$.

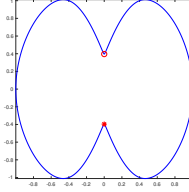


FIGURE 28. A concave 2-symmetric domain.

$$\begin{aligned} \lambda_0 = 0.5, \quad \lambda_1 = 0.3676, \quad \lambda_2 = -0.3676, \quad \lambda_3 = 0.3303, \\ \lambda_4 = -0.3303, \quad \lambda_5 = 0.2347, \quad \lambda_6 = -0.2347. \end{aligned} \quad (5.24)$$

Fig. 29 plots the eigenfunctions, their conormal derivatives and the associated single-layer potentials, respectively, associated with the eigenvalues $\lambda_1 = 0.3676$ and $\lambda_3 = 0.3303$. The numerical results clearly support our earlier assertion about the NP eigenfunctions associated with simple positive eigenvalues.

Fig. 30 plots the eigenfunctions, their conormal derivatives and the associated single-layer potentials, respectively, associated with the eigenvalues $\lambda_2 = -0.3676$ and $\lambda_4 = -0.3303$. The numerical results clearly support our earlier assertion about the NP eigenfunctions associated with simple negative eigenvalues.

Fig. 31 plots the eigenfunctions with respect to arc length for the eigenvalues $\lambda_1 = 0.3676$ and $\lambda_2 = -0.3676$ with different maximum curvature 500, 1000 and 1500.

We next investigate the blow-up rate of the NP eigenfunction or its conormal derivative with respect to the curvature. Therefore we plot the logarithm of the derivative of the absolute value of the eigenfunctions at the high-curvature point for the positive eigenvalues λ_1 , λ_3 and λ_5 , and the logarithm of the absolute value of the eigenfunctions at the high-curvature point for the negative eigenvalues λ_2 , λ_4 and λ_6 at the high-curvature point x_* with respect to different curvature in Fig. 32. It turns out that blow-up rate

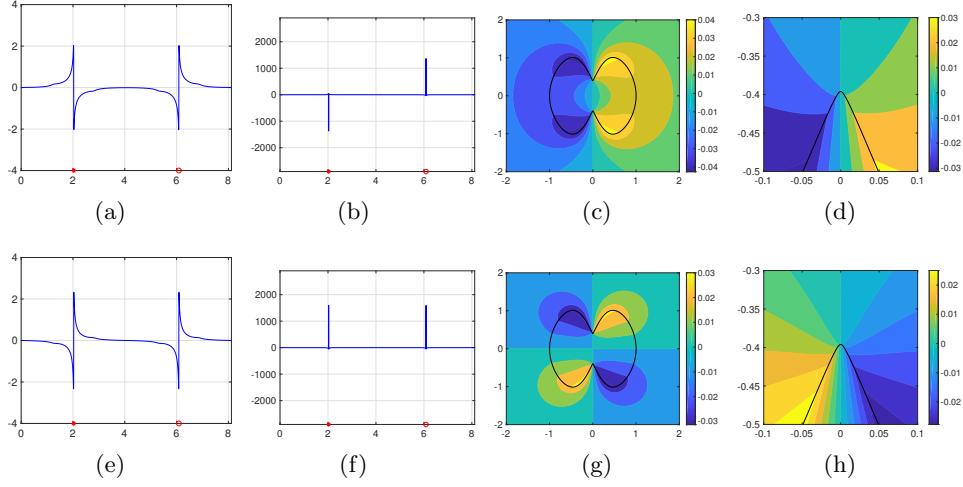


FIGURE 29. (a), (b), (c), (d). The eigenfunction, its conormal derivative, and the corresponding single-layer potential associated with $\lambda_1 = 0.3676$; (e), (f), (g), (h). The corresponding items associated with $\lambda_3 = 0.3303$.

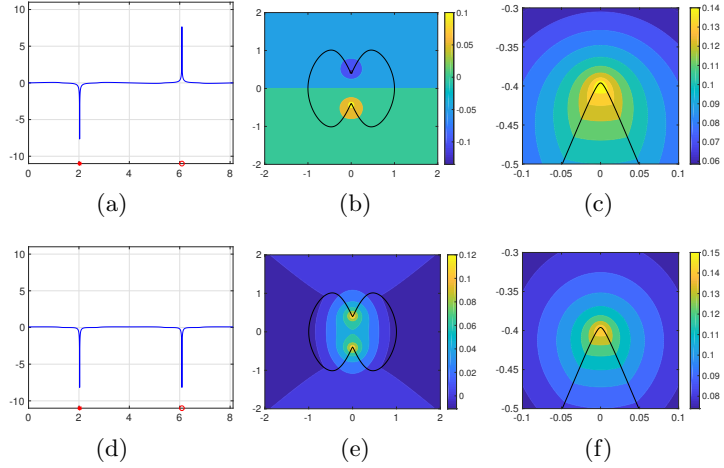


FIGURE 30. (a), (b), (c). The eigenfunction, its conormal derivative, and the corresponding single-layer potential associated with $\lambda_2 = -0.3676$; (d), (e), (f). The corresponding items associated with $\lambda_4 = -0.3303$.

also follows the rule in (5.16). By regression, we numerically determine the corresponding parameters for those different eigenvalues in (5.24), and they are listed in Table 5.

5.7. A non-symmetric domain. In this subsection, we consider a non-symmetric domain as shown in Fig. 33, which possesses three boundary points with relatively large curvatures that are marked as x_o , x_* and x_Δ in the figure. The corresponding curvatures at those three points are respectively given as

$$\kappa_{x_o} = 500, \quad \kappa_{x_*} = \kappa_{x_\Delta} = 41. \quad (5.25)$$

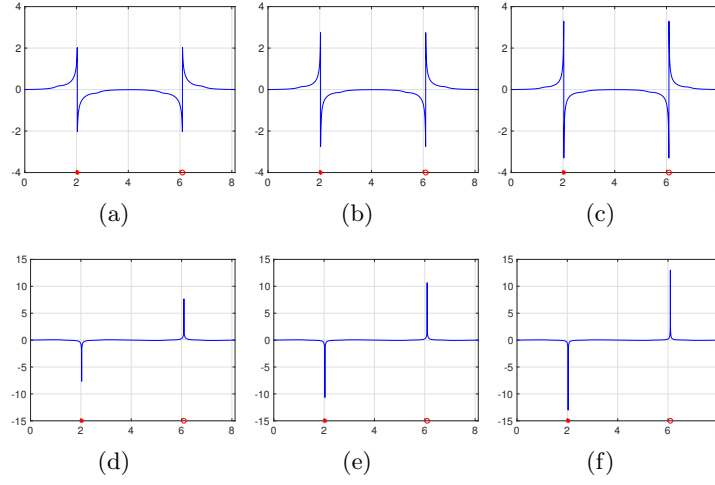


FIGURE 31. (a), (b), (c). Plotting the eigenfunctions for the positive eigenvalues $\lambda_1 = 0.3676$ with different maximum curvature 500, 1000 and 1500. (d), (e), (f). The corresponding items for the negative eigenvalue $\lambda_2 = -0.3676$.

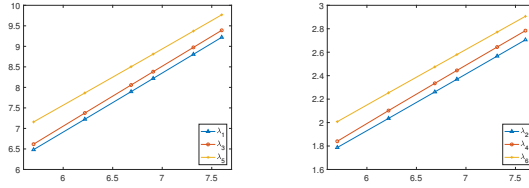


FIGURE 32. The logarithm of the absolute value of the derivative of the eigenfunction at the high-curvature point is the largest for the positive eigenvalues λ_1 , λ_3 and λ_5 and the logarithm of the absolute value of the eigenfunction at the high-curvature point for the negative eigenvalues λ_2 , λ_4 and λ_6 with respect to different curvature.

(a)				(b)			
	λ_1	λ_3	λ_5		λ_2	λ_4	λ_6
p	1.4415	1.4604	1.3742	p	0.4836	0.4963	0.4729
$\ln(\alpha)$	-1.7389	-1.7075	-0.6801	$\ln(\alpha)$	-0.9712	-0.9860	-0.6875

TABLE 5. The parameters of the form (5.16) from the regression associated with the eigenvalues in (5.24): (a) $\lambda_j, j = 1, 3, 5$; (b) $\lambda_j, j = 2, 4, 6$.

It is noted that the domain in Fig. 33 is different from the one in Fig. 11. Here, we modify the curvatures at the two points x_* and x_Δ such that the domain is no longer symmetric. Obviously, x_o is the high-curvature point.

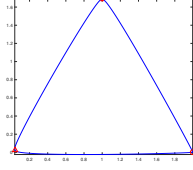


FIGURE 33. A non-symmetric domain.

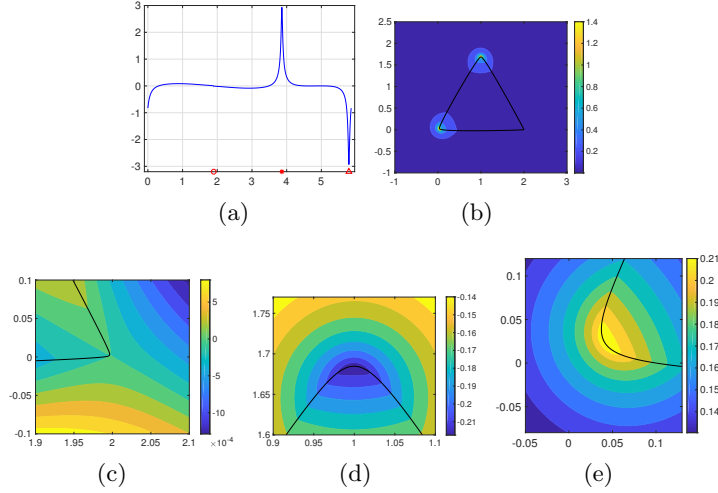


FIGURE 34. (a). Eigenfunction with respect to the arc length associated to the eigenvalue $\lambda_3 = 0.2320$; (b). The corresponding single-layer potential; (c), (d), (e). The single-layer potential around the three points x_o , x_* and x_Δ , respectively.

First, the first five largest NP eigenvalues (in terms of the absolute value) associated with ∂D in Fig. 33 are numerically found to be

$$\lambda_0 = 0.5, \quad \lambda_1 = 0.2710, \quad \lambda_2 = -0.2710, \quad \lambda_3 = 0.2320, \quad \lambda_4 = -0.2320. \quad (5.26)$$

Fig. 34 plots the eigenfunction and the corresponding single-layer potential around the three points x_o , x_* and x_Δ associated to the eigenvalue $\lambda_3 = 0.2320$. It can be readily seen that the blow-up behaviour does not occur at the high-curvature point x_o , and instead it occurs at the two points x_* and x_Δ which possesses relatively large curvatures.

Fig. 35 plots the eigenfunction, and its conormal derivative as well as the corresponding single-layer potential associated to the eigenvalue $\lambda_4 = -0.2320$. It can be readily seen that the blow-up behaviour of the conormal derivative does not occur at the high-curvature point x_o , and instead it occurs at the two points x_* and x_Δ again.

Clearly, the previous two examples show that the blow-up behaviour does not follow the one observed for symmetric domains. The two points x_* and x_Δ are symmetric with respect to x_o , and they two may compete with the point x_o to form the blow-up behaviours as observed above. However, there are no definite rules for this.

5.8. Another non-symmetric domain. In this subsection, we consider a non-symmetric domain as shown in Fig. 36, which possesses three boundary points with relatively large curvatures that are marked as x_o , x_* and x_Δ in the figure. The corresponding curvatures

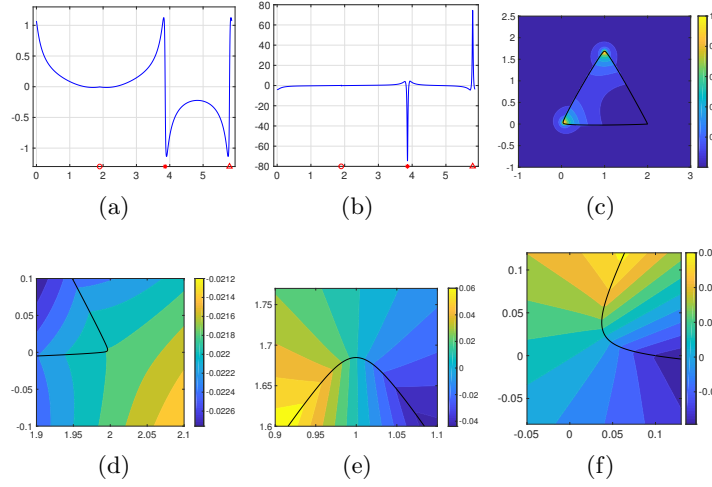


FIGURE 35. (a), (b). Eigenfunction and its conormal derivative with respect to the arc length associated to the eigenvalue $\lambda_4 = -0.2320$; (c), (d), (e), (f). The corresponding single-layer potential as well as their behaviours around the three points x_o , x_* and x_Δ , respectively.

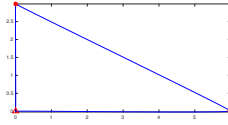


FIGURE 36. The boundary with three high-curvature points.

at those three points are respectively given as

$$\kappa_{x_o} = 500, \quad \kappa_{x_*} = 804 \quad \text{and} \quad \kappa_{x_\Delta} = 400. \quad (5.27)$$

First, the first three largest NP eigenvalues (in terms of the absolute value) associated with ∂D in Fig. 36 are numerically found to be

$$\lambda_0 = 0.5, \quad \lambda_1 = 0.3792, \quad \lambda_2 = -0.3792. \quad (5.28)$$

Fig. 37 plots the eigenfunction and the corresponding single-layer potential around the three points x_o , x_* and x_Δ associated to the eigenvalue $\lambda_1 = 0.3792$. It can be readily seen that even if the curvature at the points x_o and x_* has the relationship

$$\kappa_{x_o} < \kappa_{x_*},$$

given in (5.27), in the Fig. 37, the figure *a* shows that the absolute value of the eigenfunction φ at the point x_o is larger than that at the point x_* , namely

$$\varphi(x_o) > \varphi(x_*).$$

As for the single layer potential $S_{\partial D}[\varphi]$, *b*, *c* and *d* show that

$$S_{\partial D}[\varphi](x_o) > S_{\partial D}[\varphi](x_*).$$

Therefore for the non-symmetric domain D , the larger curvature point does not yield the larger value of the eigenvalue and the associated single layer potential for the positive eigenvalue.

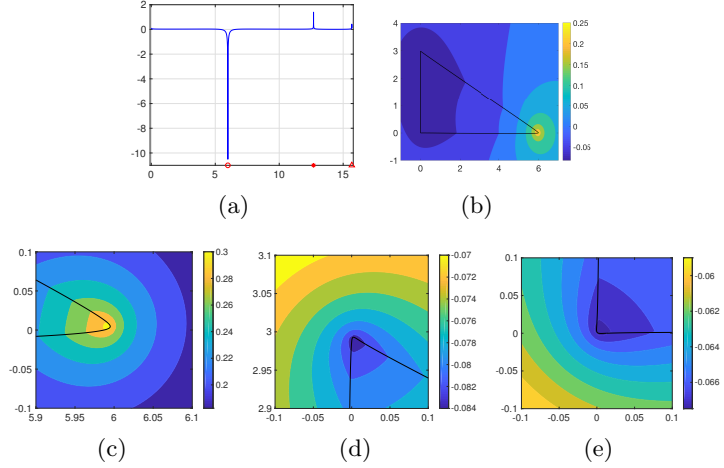


FIGURE 37. (a). Eigenfunction with respect to the arc length associated to the eigenvalue $\lambda_1 = 0.3792$; (b). The corresponding single-layer potential; (c), (d), (e). The single-layer potential around the three points x_o , x_* and x_Δ , respectively.

Fig. 38 plots the eigenfunction, and its conormal derivative as well as the corresponding single-layer potential associated to the eigenvalue $\lambda_2 = -0.3792$. It can be readily seen that even if the curvature at the points x_o and x_* has the relationship

$$\kappa_{x_o} < \kappa_{x_*},$$

from the figure *a* and *b*, the values of the derivative of the eigenfunction at the high-curvature points x_o and x_* satisfy

$$d\varphi(x_o) > d\varphi(x_*).$$

Therefore for the non-symmetric domain D , the larger curvature point does not yield the larger value of the conormal derivative of the eigenvalue for the negative eigenvalue.

6. CONCLUDING REMARKS

In this paper, we show that the Neumann-Poincaré eigenfunctions possess certain delicate and intriguing geometric structures. The results are of independent interest and significant importance in the spectral theory for the Neumann-Poincaré operator. It also opens up an exciting new field for further developments. Furthermore, the results can be used to explain the localization and geometrization phenomenon in the plasmon resonances, which is another novel and intriguing discovery made in the present article. The localization and geometrization phenomenon might be used to produce super-resolution effect in wave imaging. To illustrate this, we present a last numerical example. Consider a plasmonic inclusion D as plotted in Fig. 39, whose parametrization is given by

$$r(\theta) = 1 + 0.0001e^{8\sin(12\theta)}. \quad (6.1)$$

There are 12 cusped points and we denote that by $r_{\max}\hat{x}_n$, $n = 0, 1, \dots, 11$, where

$$r_{\max} = 1 + 0.0001e^8, \quad \hat{x}_n = \hat{x}(\pi/24 + n\pi/6), \quad n = 0, 1, \dots, 11.$$

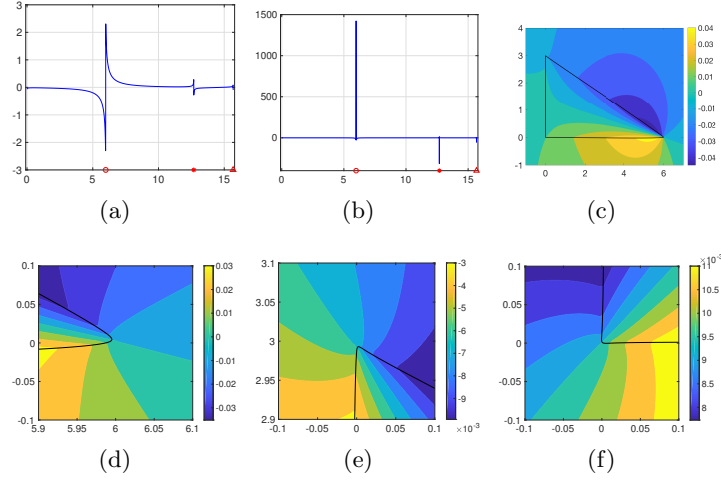


FIGURE 38. (a), (b). Eigenfunction and its conormal derivative with respect to the arc length associated to the eigenvalue $\lambda_2 = -0.3792$; (c), (d), (e), (f). The corresponding single-layer potential as well as their behaviours around the three points x_o , x_* and x_Δ , respectively.

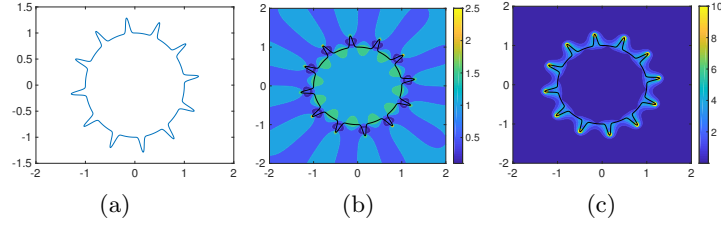


FIGURE 39. Left. A star-shaped plasmonic inclusion; Middle. Modulus of the resonant field; Right. Modulus of the gradient of the field.

It is easily seen that the distance \tilde{d} between two cusped points is

$$\tilde{d} = |r(\max)\hat{x}_n - r(\max)\hat{x}_{n+1}| = 0.6719. \quad (6.2)$$

Now, let us choose the plasmon parameters inside the domain D as follows,

$$\epsilon_c = -2.48907 \quad \text{and} \quad \delta = 0.00001,$$

which follows the rule in (2.13), since one of the NP eigenvalues of the operator $K_{\partial D}^*$ can be numerically determined to be

$$\lambda = 0.21339.$$

We also take an incident plane wave of the form (3.14) with the wave number k replaced by $k = 0.01$. By our earlier discussion on the localization and geometrization in plasmon resonances, it can be observed that strong resonant behaviours occur around the cusped points which possess very large curvatures. Those resonant behaviours can apparently be used to locate those cusp parts on the plasmonic inclusion. However, we note that the underlying wavelength is given by

$$\lambda = 2\pi/k = 628.32,$$

which is much bigger than \tilde{d} in (6.2). Hence, one might expect to have a certain super-resolution imaging effect. In this last example, we also note that $k \cdot \text{diam}(D) \approx 0.02$, which means that the localization and geometrization phenomenon occurs at an even finer scale in the quasi-static regime. Clearly, this is mainly due to the peculiar geometric structures of the NP eigenfunctions near high-curvature points. We shall investigate these intriguing problems in our future study.

ACKNOWLEDGEMENT

The work of H Liu was supported by the FRG fund from Hong Kong Baptist University and the Hong Kong RGC grants (projects 12302017 and 12302018).

REFERENCES

- [1] H. Ammari, G. Ciraolo, H. Kang, H. Lee, and G.W. Milton, *Spectral theory of a Neumann-Poincaré-type operator and analysis of cloaking due to anomalous localized resonance*, Arch. Ration. Mech. Anal., **208** (2013), 667–692.
- [2] H. Ammari, G. Ciraolo, H. Kang, H. Lee, and G.W. Milton, *Spectral theory of a Neumann-Poincaré-type operator and analysis of cloaking due to anomalous localized resonance II*, Contemporary Math., **615** (2014), 1–14.
- [3] H. Ammari, Y. Deng and P. Millien, *Surface plasmon resonance of nanoparticles and applications in imaging*, Arch. Ration. Mech. Anal., **220** (2016), 109–153.
- [4] H. Ammari, P. Millien, M. Ruiz and H. Zhang, *Mathematical analysis of plasmonic nanoparticles: the scalar case*, Archive for Rational Mechanics and Analysis, **224** (2017), 597–658.
- [5] H. Ammari, M. Ruiz, S. Yu and H. Zhang, *Mathematical analysis of plasmonic resonances for nanoparticles: the full Maxwell equations*, preprint, arXiv:1511.06817
- [6] K. Ando, Y. Ji, H. Kang, K. Kim and S. Yu, *Spectral properties of the Neumann-Poincaré operator and cloaking by anomalous localized resonance for the elastostatic system*, preprint, European J. Appl. Math., in press, 2017.
- [7] K. Ando, Y. Ji, H. Kang, K. Kim and S. Yu, *Cloaking by anomalous localized resonance for linear elasticity on a coated structure*, SIAM J. Math. Anal., in press, 2017.
- [8] K. Ando, H. Kang and H. Liu, *Plasmon resonance with finite frequencies: a validation of the quasi-static approximation for diametrically small inclusions*, SIAM J. Appl. Math., **76** (2016), 731–749.
- [9] K. Ando, H. Kang and Y. Miyanishi, *Elastic Neumann-Poincaré operators on three dimensional smooth domains: Polynomial compactness and spectral structure*, Int. Math. Res. Notices, in press, 2017.
- [10] K. Ando, H. Kang and Y. Miyanishi, *Spectral structure of elastic Neumann-Poincaré operators*, preprint
- [11] E. Blåsten and H. Liu, *Scattering by curvatures, radiationless sources, transmission eigenfunctions and inverse scattering problems*, arXiv: 1808.01425
- [12] G. Bouchitté and B. Schweizer, *Cloaking of small objects by anomalous localized resonance*, Quart. J. Mech. Appl. Math., **63** (2010), 438–463.
- [13] O.P. Bruno and S. Lintner, *Superlens-cloaking of small dielectric bodies in the quasistatic regime*, J. Appl. Phys., **102** (2007), 124502.
- [14] D. Chung, H. Kang, K. Kim and H. Lee, *Cloaking due to anomalous localized resonance in plasmonic structures of confocal ellipses*, SIAM J. Appl. Math., **74** (2014), no. 5, 1691–1707.
- [15] Y. Deng, H. Li and H. Liu, *On spectral properties of Neumann-Poincaré operator and plasmonic cloaking in 3D elastostatics*, J. Spectral Theory, in press.
- [16] J. Helsing, H. Kang and M. Lim, *Classification of spectra of the Neumann-Poincaré operator on planar domains with corners by resonance*, Ann. I. H. Poincaré-AN, **34** (2017), 991–1011.
- [17] J. Helsing and K. M. Perfekt, *The spectra of harmonic layer potential operators on domains with rotationally symmetric conical points*, J. Math. Pures Appl., in press, DOI: 10.1016/j.matpur.2017.10.012
- [18] Y. Ji and H. Kang, *A concavity condition for existence of a negative Neumann-Poincaré eigenvalue in three dimensions*, arXiv:1808.10621
- [19] H. Kang and D. Kawagoe, *Surface Riesz transforms and spectral property of elastic Neumann-Poincaré operators on less smooth domains in three dimensions*, arXiv:1806.02026

- [20] H. Kang, M. Lim and S. Yu, *Spectral resolution of the Neumann-Poincaré operator on intersecting disks and analysis of plasmon resonance*, Arch. Rati. Mech. Anal., **226** (2017), 83–115.
- [21] H. Kettunen, M. Lassas and P. Ola, *On absence and existence of the anomalous localized resonance without the quasi-static approximation*, SIAM J. Appl. Math., **78** (2018), 609–628.
- [22] D. M. Kochmann and G. W. Milton, *Rigorous bounds on the effective moduli of composites and inhomogeneous bodies with negative-stiffness phases*, J. Mech. Phys. Solids, **71** (2014), 46–63.
- [23] R.V. Kohn, J. Lu, B. Schweizer and M.I. Weinstein, *A variational perspective on cloaking by anomalous localized resonance*, Comm. Math. Phys., **328** (2014), 1–27.
- [24] R.S. Lakes, T. Lee, A. Bersie, and Y. Wang, *Extreme damping in composite materials with negative-stiffness inclusions*, Nature, **410** (2001), 565–567.
- [25] H. Li and H. Liu, *On anomalous localized resonance for the elastostatic system*, SIAM J. Math. Anal., **48** (2016), 3322–3344.
- [26] H. Li and H. Liu, *On three-dimensional plasmon resonance in elastostatics*, Annali di Matematica Pura ed Applicata, **196** (2017), 1113–1135.
- [27] H. Li and H. Liu, *On anomalous localized resonance and plasmonic cloaking beyond the quasistatic limit*, Proceedings A, at press, 2018.
- [28] H. Li, J. Li and H. Liu, *On quasi-static cloaking due to anomalous localized resonance in \mathbb{R}^3* , SIAM J. Appl. Math., **75** (2015), no. 3, 1245–1260.
- [29] H. Li, J. Li and H. Liu, *On novel elastic structures inducing plasmon resonances with finite frequencies and cloaking due to anomalous localized resonance*, J. Math. Pures Appl., DOI:10.1016/j.matpur.2018.06.014
- [30] H. Li, S. Li, H. Liu and X. Wang, *Analysis of electromagnetic scattering from plasmonic inclusions at optical frequencies*, arXiv:1804.09517
- [31] R.C. McPhedran, N.-A.P. Nicorovici, L.C. Botten and G.W. Milton, *Cloaking by plasmonic resonance among systems of particles: cooperation or combat?* C.R. Phys., **10** (2009), 391–399.
- [32] D. A. B. Miller, *On perfect cloaking*, Opt. Express, **14** (2006), 12457–12466.
- [33] G.W. Milton and N.-A.P. Nicorovici, *On the cloaking effects associated with anomalous localized resonance*, Proc. R. Soc. A, **462** (2006), 3027–3059.
- [34] G.W. Milton, N.-A.P. Nicorovici, R.C. McPhedran, K. Cherednichenko and Z. Jacob, *Solutions in folded geometries, and associated cloaking due to anomalous resonance*, New. J. Phys., **10** (2008), 115021.
- [35] J. C. Nédélec, *Acoustic and Electromagnetic Equations*, Applied Mathematical Sciences 144, 2001, Springer-Verlag, New York.
- [36] H. Nguyen, *Cloaking via anomalous localized resonance for doubly complementary media in the finite frequency regime*, arXiv:1511.08053.
- [37] N.-A.P. Nicorovici, R.C. McPhedran, S. Enoch and G. Tayeb, *Finite wavelength cloaking by plasmonic resonance*, New. J. Phys., **10** (2008), 115020.
- [38] N.-A.P. Nicorovici, R.C. McPhedran and G.W. Milton, *Optical and dielectric properties of partially resonant composites*, Phys. Rev. B, **49** (1994), 8479–8482.
- [39] N.-A.P. Nicorovici, G.W. Milton, R.C. McPhedran and L.C. Botten, *Quasistatic cloaking of two-dimensional polarizable discrete systems by anomalous resonance*, Optics Express, **15** (2007), 6314–6323.
- [40] G.W. Milton and N.-A.P. Nicorovici, *On the cloaking effects associated with anomalous localized resonance*, Proc. R. Soc. A, **462** (2006), 3027–3059.
- [41] J. B. Pendry, *Negative refraction makes a perfect lens*, Phys. Rev. Lett., **85** (2000), 3966.
- [42] D. R. Smith, J. B. Pendry and M. C. K. Wiltshire, *Metamaterials and negative refractive index*, Science, **305** (2004), 788–792.
- [43] V. G. Veselago, *The electrodynamics of substances with simultaneously negative values of ϵ and μ* , Sov. Phys. Usp., **10** (1968), 509.

HELSINKI, FINLAND.

E-mail address: `eemeli@countermail.com`

DEPARTMENT OF MATHEMATICS, HONG KONG BAPTIST UNIVERSITY, KOWLOON, HONG KONG SAR.

E-mail address: `hongjie_li@yeah.net`

DEPARTMENT OF MATHEMATICS, HONG KONG BAPTIST UNIVERSITY, KOWLOON, HONG KONG SAR.

E-mail address: `hongyu.liuip@gmail.com`, `hongyuliu@hkbu.edu.hk`

DEPARTMENT OF MATHEMATICS, HONG KONG BAPTIST UNIVERSITY, KOWLOON, HONG KONG SAR.

E-mail address: `yuliang@hkbu.edu.hk`